University of New Mexico
UNM Digital Repository

Mechanical Engineering ETDs | Engineering ETDs

1-30-2013

Mechanical and electrical fatigue of aerosol jet printed conductors

Adam Cook

Follow this and additional works at: https://digitalrepository.unm.edu/me_etds

Recommended Citation
Cook, Adam. "Mechanical and electrical fatigue of aerosol jet printed conductors." (2013). https://digitalrepository.unm.edu/me_etds/66

This Thesis is brought to you for free and open access by the Engineering ETDs at UNM Digital Repository. It has been accepted for inclusion in Mechanical Engineering ETDs by an authorized administrator of UNM Digital Repository. For more information, please contact disc@unm.edu.

Adam W. Cook

Candidate

Mechanical Engineering

Department

This thesis is approved, and it is acceptable in quality and form for publication:

Approved by the Thesis Committee:

Dr. Tariq Khraishi , Chairperson

Dr. Christopher Apblett

Dr. Yu-Lin Shen

MECHANICAL AND ELECTRICAL FATIGUE OF AEROSOL JET PRINTED CONDUCTORS

by

ADAM W. COOK

B.S., UNIVERSITY OF NEW MEXICO

THESIS

Submitted in Partial Fulfillment of the
Requirements for the Degree of

Master of Science

Mechanical Engineering

The University of New Mexico
Albuquerque, New Mexico

December, 2012

DEDICATION

Para la familia Cook

ACKNOWLEDGMENTS

Without the support of my committee members, this thesis would not have been possible. I would like to thank Dr. Tariq Khraishi for his guidance, mentorship, and warm welcome to his research group, Dr. Yu-Lin Shen for his service and input on my committee, and my long-term mentor and friend, Dr. Christopher Apblett. Chris, you have given me an amazing set of tools which I will utilize throughout my career as an engineer. Thank you for your support and encouragement.

I would also like to acknowledge my many friends and collogues at the AML for their support. Special thanks are extended to Dr. Leo Small, Dr. Timothy Boyle, and Jeff Salzbrenner for their invaluable assistance, guidance, and advice. Your individual contributions to the success of my work have been greatly appreciated. I further extend my gratefulness to Bonnie McKenzie, and Dr. Edward Cole for their assistance in optical and qualitative analysis.

I thank my family and especially my parents, Judy and Kyle, for their love and understanding. You have always been a constant source of inspiration to Erin and me. Thank you for teaching us how to work for what. To my sister Erin, I win! Love ya' lots! Lastly, I express my most heartfelt appreciation to my wife Felicha for her unconditional love over our many years together. Your patients and calmness throughout *our* scholastic endeavors has been greatly appreciated. I promise to never take advantage of the love and companionship that you have given me so generously over the years. Together we have learned that "These walls are funny. First you hate 'em, then you get used to em'. Enough time passes, you get so you depend on them." Remember my love, "Salvation lies within."

MECHANICAL AND ELECTRICAL FATIGUE OF AEROSOL JET PRINTED CONDUCTORS

by

Adam W. Cook

B.S., Mechanical Engineering, University of New Mexico, 2008
M.S., Mechanical Engineering, University of New Mexico, 2012

ABSTRACT

Non-contact metallization processes, such as aerosol jet printing, allows for the deposition and novel processing of nanoparticle based conductive circuitry. The primary advantages in the utilization of such methods include the minimization of substrate handling and the exploitation of nanomaterial's ability to form electrically conductive pathways at temperatures as low as 80°C. Applying non-contact deposition techniques to the manufacturing of photovoltaic components has recently gained interest but one of the potential risks are unknown aging and failure mechanisms. Fatigue characterization of printed materials has been widely studied on flexible substrates. However, research on technologically relevant silicon has been limited and presents an opening for further investigation. This thesis demonstrates that non-contact printing methods can be extremely variable and material dependent. Furthermore, accelerated conductor aging on silicon as a result of applied strain has the potential to result in the formation of cracks along a printed conductor which serves to inhibit continuity in a printed device.

TABLE OF CONTENTS

LIST OF FIGURES

LIST OF TABLES

Introduction:

The continuous and global demand for low cost and renewable energy has long identified photovoltaic power generation as a viable source of energy production[1,2]. Traditionally, the metallization of solar panels as required for bus voltage lines and current collecting grids has been accomplished photo lithographically and through screen printing methods[3]. While reliable, the limits of these methods are restrictive as photovoltaic systems are miniaturized or as substrate thickness are decreased[4]. Processes such as screen printing which require substrate contact for metallization are undesirable as handling increases the risk of breakage. Furthermore, desires for inexpensive and environmentally neutral manufacturing techniques minimize lithographically-defined and evaporative metal deposition processing of components as advancements to manufacturing methods.

A variety of contactless printing methods have been developed which allow for the metallization of glass and polymer substrates while minimizing substrate handling and materials waste. Ink Jet (IJ) printing techniques allow for the continuous generation of discrete droplets from metallic fluid reservoirs[5]. Droplets ranging in diameter from 18-635 microns can be utilized to create continuous and conductive line segments suitable for photovoltaic cell construction [6]. With the development and maturation of IJ print technology, nanoparticle based materials were identified for use in solar cell fabrication. Unlike thick film inks used for the screen printing of electrical interconnections which require 400 ˚C processing to impart continuity, nano materials can be post processed to provide electrical continuity at temperatures between as 80 ˚C and 230 ˚C [1,7, 8]. Another evolving printing process for electronics and solar cell fabrication is the Aerosol Jet (AJ)

deposition technique. Akin to the IJ method, the AJ method is a contactless deposition technique that utilizes nanomaterial based inks to precisely deposit printed conductors on a substrate[9]. AJ differs from droplet-on-demand systems in that a jet is comprised of many tiny droplets rather than a single droplet. A coaxial stream of nanoparticle material sheathed by an annular gas envelope allows focusing of the stream of droplets and good line definition upon deposition on a substrate. As deposited, discrete metallic nanoparticles are nonconductive. With thermal post processing, it is possible to sinter the deposited nanoparticles to form conductive pathways. As an example, Zhao et. al, Figure 1, show pre and post processed silver nanoparticle ink depositions using the aerosol jet method[10].

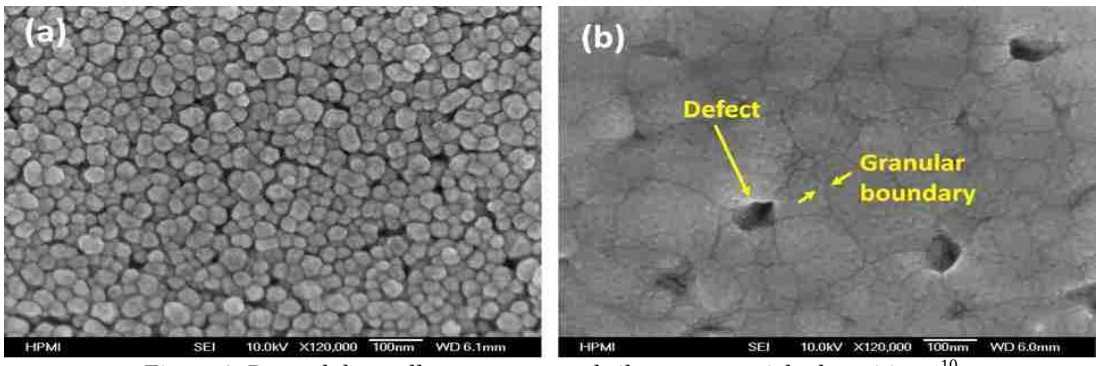

Figure 1: Pre and thermally post processed silver nanoparticle depositions.[10]

The depositions produced electrically conductive pathways having bulk resistivities of 4.5 x 10^{-6} Ω·cm. Working distances of several millimeters are possible without significant divergence of the collimated stream of metallic nanoparticle laden gas. However, the presence of surface defects represent a potential source of conductor failure should the deposition be subject to mechanical strain, since such defects could act as a stress concentrator for the printed material during thermal or mechanical cycling.

A major advantage of the AJ printing process is that the technique is not limited to planar substrates. Micron thick depositions can be formed over topographically challenging substrates and result in minimum feature widths of 10 microns, Figure 2[11].

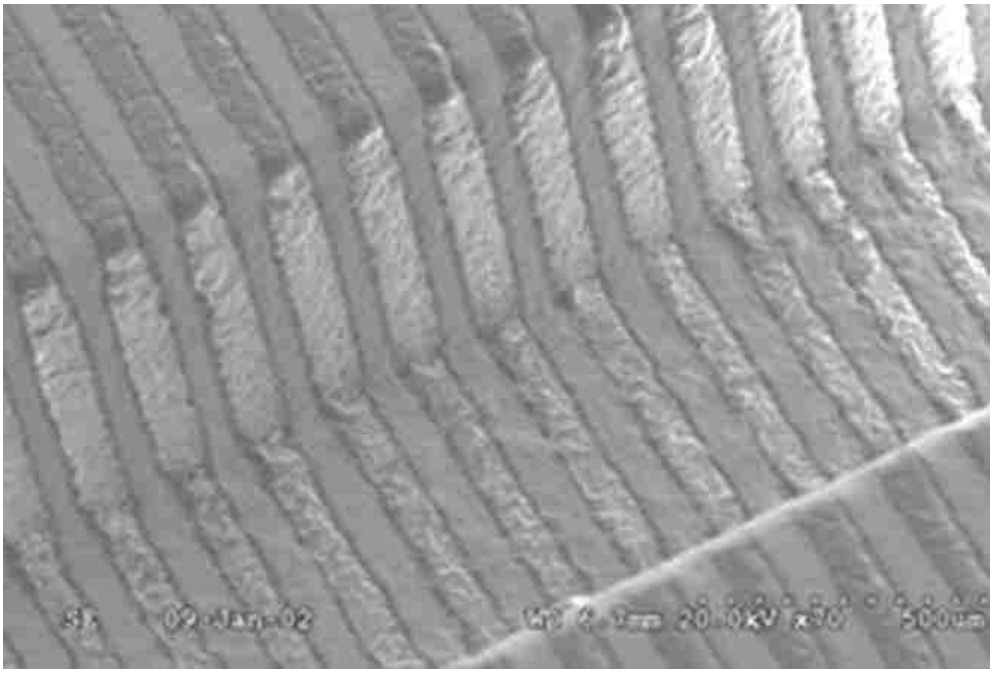

Figure 2: Aerosol Jet printed conductors over topography. Source: *Organicandprinedelectronics.com*[11]

Additionally, the AJ method is well suited for seed layer printing and subsequent electroplating when a specific metal ink formulation is not available for direct deposition[12,13]. With advancements in printing technology and materials development, alternative manufacturing techniques for solar cell fabrication at minimized feature geometry have evolved. Yet, the long term aging behavior of printed electrical components is widely unknown as applied to solar technology. One concern that has received little attention to date has been fatigue cycling of the printed materials as they undergo flexure from panel loading or from thermal stress cycling. Traditionally,

evaluating fatigue properties of bulk metals has been relatively straight forward and is well characterized in the literature[14,15]. However, as deposited and thermally sintered metallic nanoparticle inks do not result in fully dense metal components. Bulk electrical resistivities are greater than the parent metals after sintering[16]. Once thermally post processed, a porous but conductive pathway is created which typically exhibits mechanical strengths less than a comparable bulk metal[17]. Furthermore, materials properties such as Young's Modulus are not defined for non-bulk printed metals. As such, it is difficult to apply conventional evaluation principles such as tensile testing to printed conductors. Because of this microstructure, it is likely that the fatigue and aging of printed lines will manifest very differently to that expected from well annealed, bulk samples**.**

Martynenko et al. have evaluated photo lithographically defined copper foil conductors for mechanical reliability using conventional testing methodologies. It was shown that strain and tensile stress increased as a function of displacement and, as expected, are temperature dependent in 150 micron thick polymer encapsulated foil conductors, Figure 3.

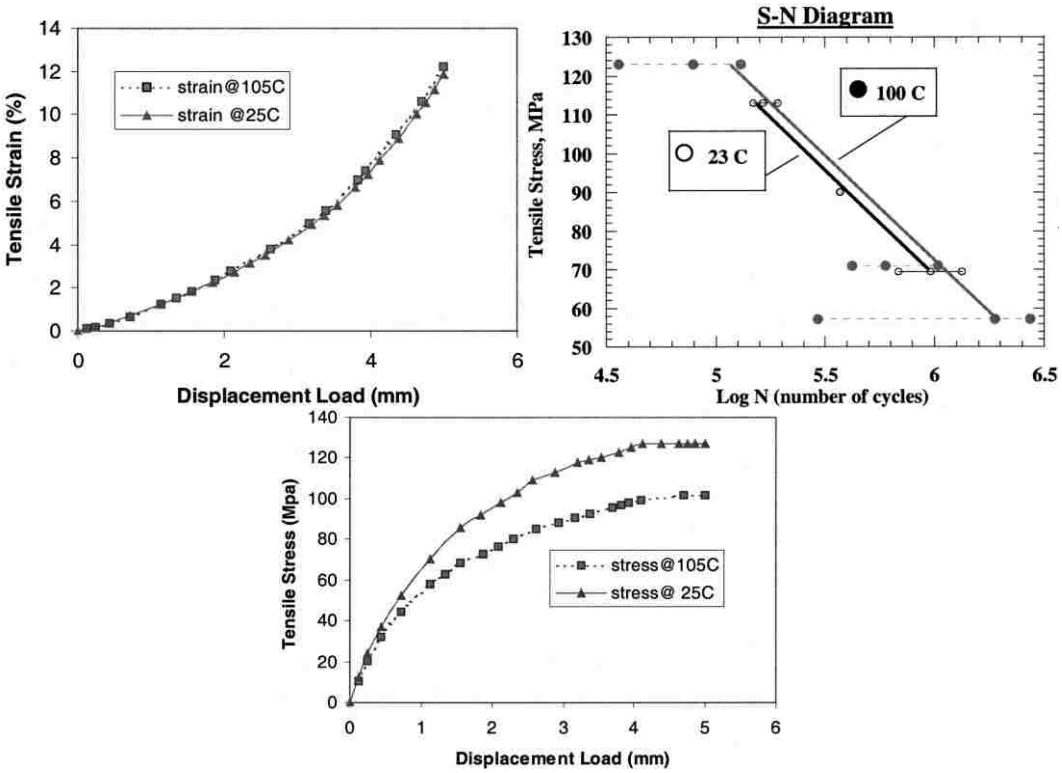

Figure 3: Strain and stress evolution at various temperatures for polymer encapsulated copper foil conductors as shown by Martynenko et. al.[18]

Furthermore, optical analysis revealed crack formation in the foils but did not address any changes in electrical resistivity that may have resulted as a consequence of mechanical fatigue[18]. Wiese et. al studied copper ribbons for use as electrical interconnects in modular solar panels. Using a millimeter wide, 100 micron thick bare copper ribbon, a temperature dependent stress-strain relation was generated. Repeatable and predictable failure modes were observed and were noted to be functions of applied force, total displacement, and number of cycles[19]. As was noted with Martynenko et al., the formation of cracks in copper conductors was observed and was shown to be a potential mode of failure in solar panel assemblies.

The electrical and mechanical evaluation of IJ or AJ printed conductors is of primary concern when applied to photovoltaic applications. As noted, IJ and AJ depositions utilizing nanoparticle ink technology seldom result in equivalent conductive pathways as compared to a foil trace or wire. For this reason it will be necessary to understand the electromechanical properties for systems in which contactless print techniques have been used to deposit conductive pathways for photovoltaic applications. Utilizing an IJ deposition technique and silver nanoparticle ink formulation, Quintero et al. demonstrated that a printed samples resistance changes as a function of cycle count and strain when evaluated on polyimide film[20]. It was shown that after as few as 300,000 cycles, a 60% variation in resistance results. Scanning electron microscopy revealed morphological changes in the conductive trace post cycling which is thought to be a result of mechanical aging. With increasing cycle count, void growth in the porous IJ deposited film increased and is believed to be responsible for the printed devices resistance increases.

While the study discussed above investigated the aging properties of printed materials, there are several considerations which were neglected. The authors did not report their findings as a function of resistivity but rather resistance. While height and width data for the printed conductors was obtained, the authors chose not to correlate their measurements with that of their sample's resistivity. While this conversion results in the multiplication by a scalar quantity, it is advantageous because the measurement changes from an extrinsic property (resistance) to a materials intrinsic property (resistivity) that can be compared to tabulated values. Additionally, crack formation and electrical resistivity in IJ deposited silver nanoparticle conductors have been shown to be

functions of substrate choice and annealing temperature [21]. Using Kapton can result in lower resistivities as compared to an equivalent device printed on glass or silicon, which is pertinent to the photovoltaic application. Knowing that wetting properties differ between substrates, it is impossible to determine if substrate effects perturbed the outcome of the study. Furthermore, as the measurement techniques used in obtaining resistance data were not disclosed, it is difficult to surmise what effect, if any, Joule heating had on the printed samples resistivity.[22]

Since strain in the printed materials will be of consequence to their aging, it is reasonable to look to the literature for examples in which thin film printed materials have been subjected to strain, such as in the printed sensor literature. The ability to directly print strain sensors as shown by Quintero et al. was elaborated on by Maiwald et al. Using a silver nanoparticle based ink and subsequent thermal post processing at 350˚C, a conductors bulk resistivity was shown to be 70% of that of pure silver[23]. Over a period of 10 hours at 350 ˚C, the printed samples conductivity was stable and the resulting temperature coefficient of resistivity was determined to be 3.06×10^{-3} K^{-1}, slightly lower than that of pure silver. Tensile and compressive testing on insulated aluminum substrates at 0.5Hz and 500-1000 Newton loadings produced reliable and repeatable gauge factor changes to 1000 cycles.

This study demonstrated the ability to directly print strain gauges on insulated metallic substrates. However, the conventional testing methodology did not provide any insight into the long term fatigue and mechanical aging of printed devices or interconnections. While SEM was performed on as-printed and sintered inks, a

comparison with post cycled samples was not carried out. Consequently, little is known about any morphological changes which may occur as a result of cyclic loading.
The effects of cyclic loadings on solar panels and their printed components as a result of temperature variations throughout a day should be considered as a potential source of failure. In addition to sunrise and sunset, significant temperature variation can result as consequence of passing cloud formations and strong winds. Having shown printed materials only approximate physical properties of bulk metals, it is necessary to directly evaluate electrical response at varying temperature conditions to ensure long term reliability in IJ or AJ printed devices. Additionally, microscopy of pre and post cycled printed devices will allow for the evaluation of mechanical aging which may result from high cycle count loadings.

Based on the benefits of using AJ printed materials as current collectors for photovoltaics, and the need to understand their long term aging effects when exposed to strain and thermal environments, this thesis seeks to study the effect of these changes on samples printed on technologically relevant Si substrates. An observed effect, if any, will provide insight as to the suitability of the AJ printing technique as a replacement or complementary manufacturing method to screen printing in the fabrication of solar cells. Aging, as manifest by electrical changes in sample resistivity, is hypothesized to result in conductor fatigue in printed circuits and is believed to result in the formation of micro cracks under cyclic loading and across temperature profiles.

Experimental:

For a given voltage, the ability of a circuit to conduct current varies as a function of resistance. As such, it is necessary to characterize the way in which a printed conductor's resistivity may change with respect to cyclic loading at a specified rate of strain. Under ideal and static conditions one would not expect any change in the resistivity of a printed circuit. However, with constant loading and unloading in a printed system resulting from environmental phenomenon, it is reasonable to hypothesize that printed circuitry may experience changes in resistivity resulting from mechanical fatigue and crack formation.

The determination of an appropriate testing methodology for conductors deposited on silicon was undertaken prior to the material properties evaluation of printed conductors. Axial testing of silicon systems was dismissed as a path forward for several reasons. The difficulty in fixturing 25-550 micron thick silicon strips in axial testing equipment without breakage or out of plane strain was a concern. Although commercially available test platforms capable of high cycle rate operation exist in the market place (Instron, Norwood, MA), such equipment is expensive and was not available for use at the time of testing. Furthermore, as the elasticity of silica is extremely limited, it was likely that a glass substrate would fracture under axial loading prior to mechanical fatigue of any conductor printed on the substrate.

Testing platform designs included the investigation of several cantilever beam bending methods. In one method, a silicon substrate with an integral printed circuit would have been rigidly fixed at one end and a shaft driven cam used to induce bending at the free end. The printed conductor would have leads attached to facilitate resistance

measurements. The rate of cyclic loading and strain were to be governed by rotational shaft speed and cam geometry of the motor. Any changes in conductor resistivity resulting from bending induced fatigue would be recorded in real time and logged for subsequent analysis.

A second cantilever bending beam design was explored which would utilize piezoelectric actuators to induce strain in conductors printed atop silicon substrates. Piezoelectric devices respond predictably, reliably, and rapidly to electrical impulses to produce mechanical energy. Under this design alternative, a circuit printed on silicon would be rigidly adhered to a PZT actuator and a voltage supplied to the bending motor to produce a displacement and resultant strain in the cantilever. A clear advantage in the use of a piezoelectric test platform was the simplicity involved in implementing a control system to actuate the bending beams. As opposed to the use of a servo motor based system, expensive motion controllers were not required and a control system suitable for the generation of pulsed voltage signals could be quickly implemented. The decision to design and implement a piezoelectric test platform for the evaluation of printed conductor fatigue was made. Figure 4 schematically depicts the design and layout of the selected system.

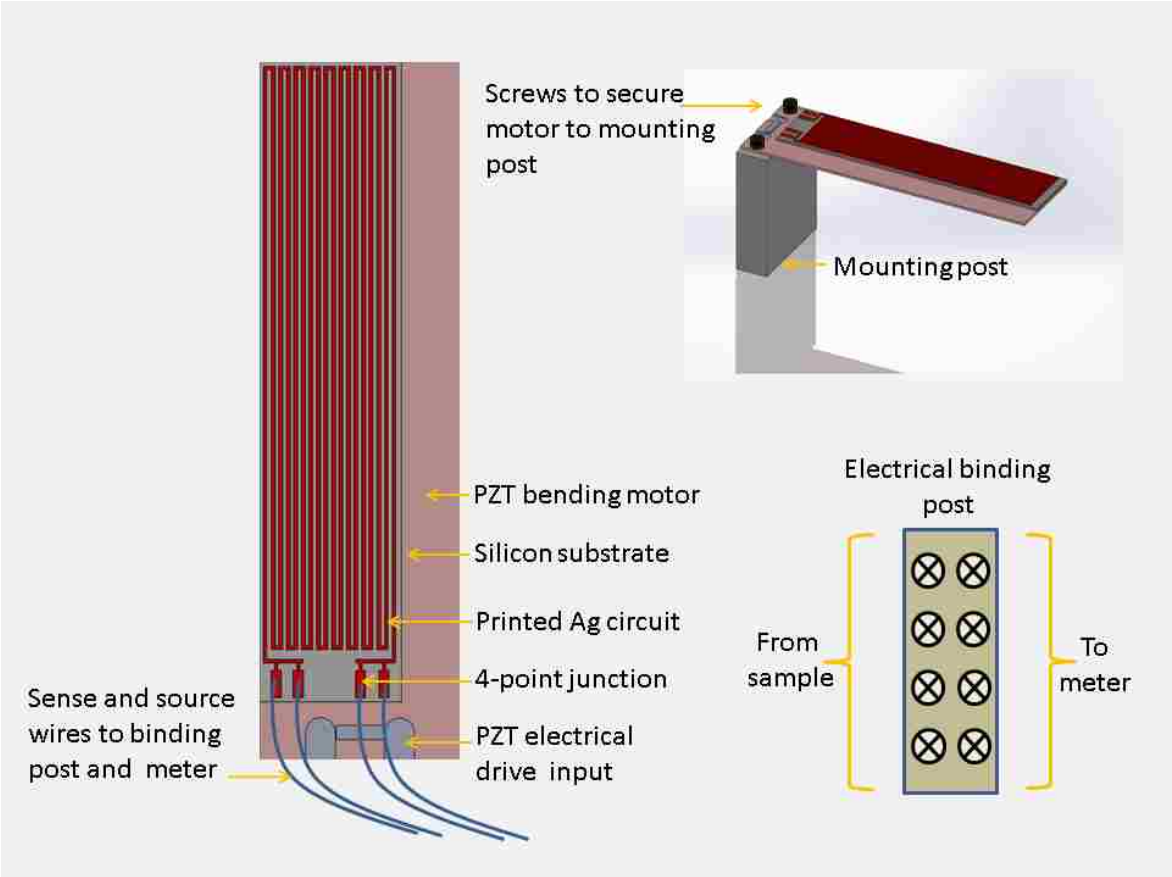

Figure 4: Schematic representation of the design and layout of the piezoelectric test platform.

Piezoelectric bending motors (Piezo Systems, Woburn, MA) were obtained and a control system designed built. Figure 5 shows the free deflection and force associated with the selection of an unloaded Q220-A4-503YB bending motor. Actual deflection was anticipated to vary as a result of silicon attachment and would need to be verified at the time of evaluation. This would be accomplished by taking displacement measurements of the beam at the free end with a non-contact laser displacement sensor.

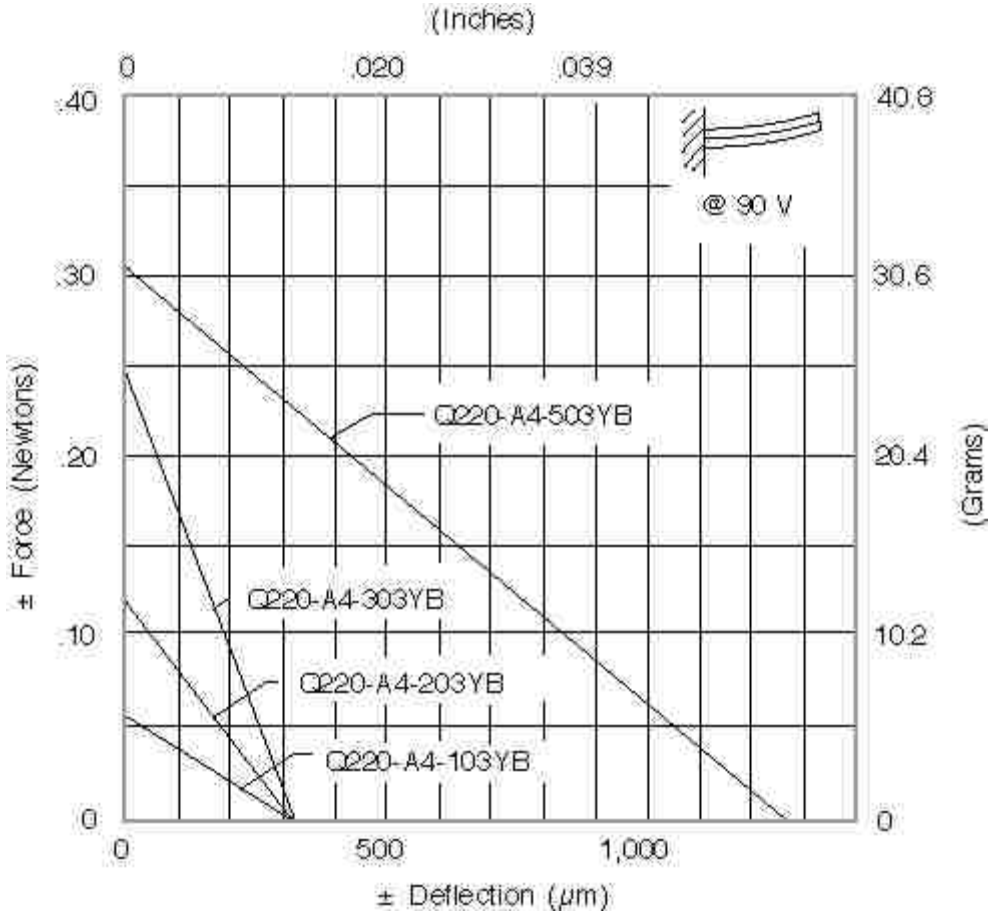

Figure 5: Deflection and force curves associated with Piezo Systems mending motors. (Manufactures data)

Using Lab View and a computer controlled power supply (Kiethly, Cleveland, Ohio) a robust control system capable of supplying +/- 90 Volt control signals to the bending motors at frequencies up to 50 Hertz was created. Further integration of digital multimeters (HP, Palo Alto, CA and Kiethly) would allow for the monitoring and logging of sample resistance changes which were suspected to occur at increasing cycle count and as a result of conductor fatigue. A laser displacement sensor (Keyence, Osaka, Japan) was integrated into the control system to provide independent displacement information which was used in the determination of strain in the substrate.

Figure 6 depicts the constructed experimental set up securely mounted to an aluminum base to be used for data acquisition.

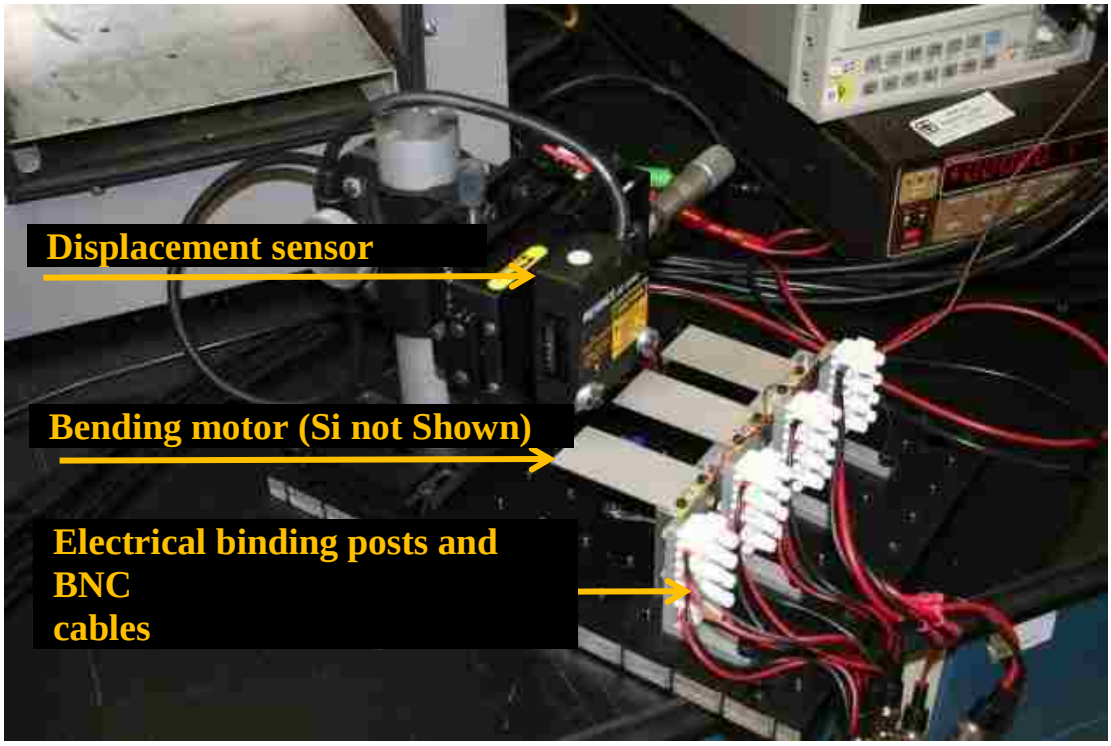

Figure 6: Piezoelectric actuator testing array permitting evaluation of three samples simultaneously. The laser displacement sensor has been rigidly fixed and binding posts implemented to provide reliable signal transfer to measurement equipment.

Lastly, the test platform was inserted into a modified oven, Figure 7, so that tests could be performed as a function of temperature. For measurement integrity, shielded BNC type cables were implemented for signal transfer from the electrical binding posts to the measurement equipment. The LabView program written for data acquisition and instrumentation control is presented in figure 8.

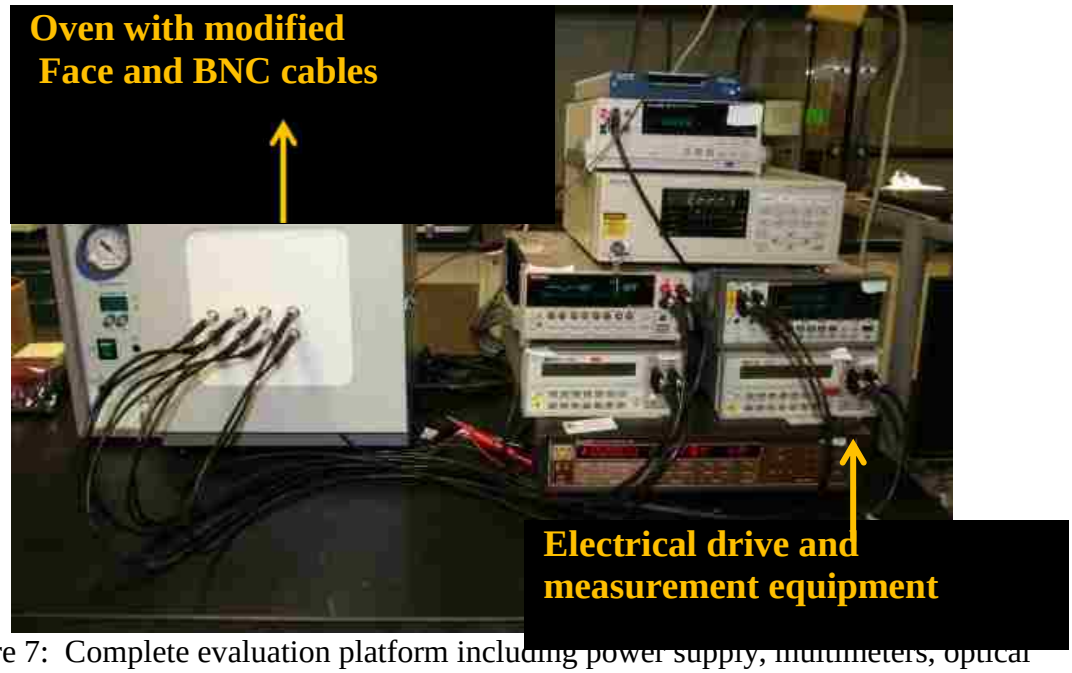

Figure 7: Complete evaluation platform including power supply, multimeters, optical displacement sensor (not visible), and oven. Note use of fully shielded coaxial cable for signal integrity.

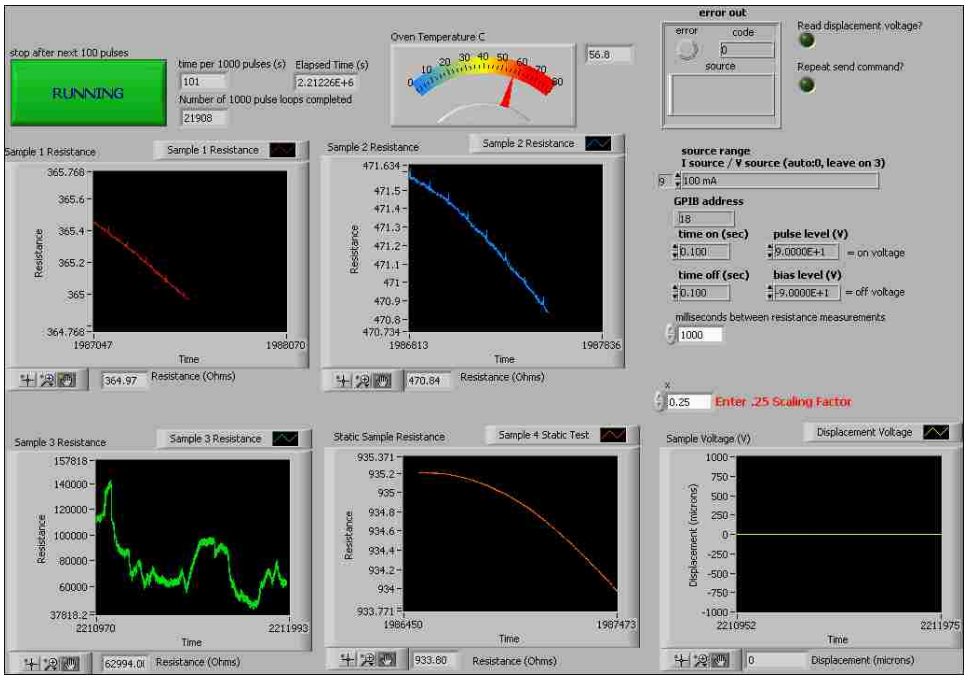

Figure 8: Graphical interface created to control evaluation parameters and allow for data acquisition.

Samples were prepared using a commercial aerosol jet system and nanoparticle ink. Utilizing an AJ deposition technique (Optomec, Albuquerque, NM) and a 40 wt% silver nanoparticle ink (UT dots, Champaign, IL), samples were printed on $[\bar{1}10]$ diced silicon substrates of thickness ranging between 25 and 550 microns (Virginia Semiconductor, Fredericksburg, VA). Aerosol Jet metallization is accomplished by ultrasonically atomizing a small aliquot of nanoparticle ink and introducing inert gas streams to transport and focus the atomized material through a 150 micron orifice. Over the duration of a 15 minute printing cycle, the ink reservoir can be depleted by as much as 15%. This process is depicted in Figure 9.

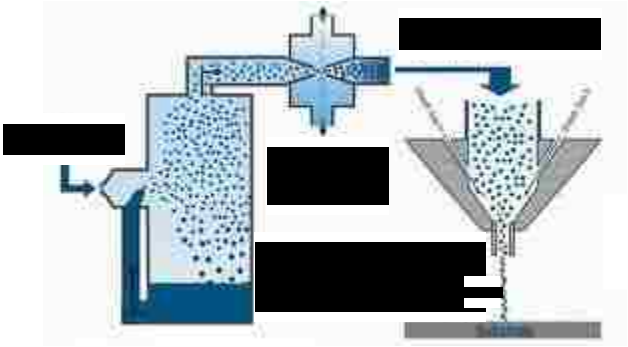

Figure 9: Aerosol Jet metallization process. Source: *Orgaincandprintedelectronics.com*[11]

Three coats of silver nanoparticle ink (necessary for even coverage and increased likely hood of conductivity) were deposited via a translating robotic stage at a rate of 5mm/sec. As a result, conductor having thickness of 1-3 microns, widths of approximately 50-160 microns, minimum cross-sectional areas between 80 and 132 square microns, and sensing lengths of 1250 millimeters were generated. The variation within and across samples is likely a function of several variables including process stability, depletion of ink from the fluid reservoir, and surface wetting effects of the ink

substrate interface. Figure 10 schematically depicts the printed geometry used for conductor fatigue evaluation.

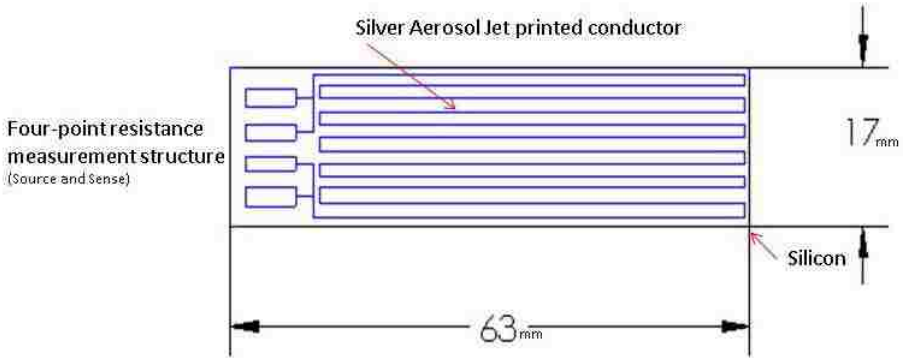

Figure 10: Schematic representation of the 1.25 meter pattern developed for fatigue evaluation

Following ink deposition, samples were thermally post processed at 170 ˚C for a period of four hours. To ensure signal integrity during testing 36AWG insulated wire leads were attached to the evaluation coupon using a thick paste silver ink (Ercon, Wareham, MA) and strain relieved with a UV curable epoxy (Loctite, Westlake OH). Furthermore, the resistance measurement performed utilized a four point technique to minimize contact resistance as well as eliminate wiring and instrumentation impedance. By sourcing a known current *I* through the printed sample, the resistance *R* was calculated as a function of sample voltage *V* and is fully defined by Ohms Law and equation 1.

$$\text{Equation 1: } R = \frac{V}{I}$$

Subsequent mounting of the printed silver conductor and silicon system to the PZT bending actuator was accomplished using cyanoacrylate (Loctite, Westlake, OH). Figure 11 depicts the assembled test coupons ready for evaluation with the constructed test platform.

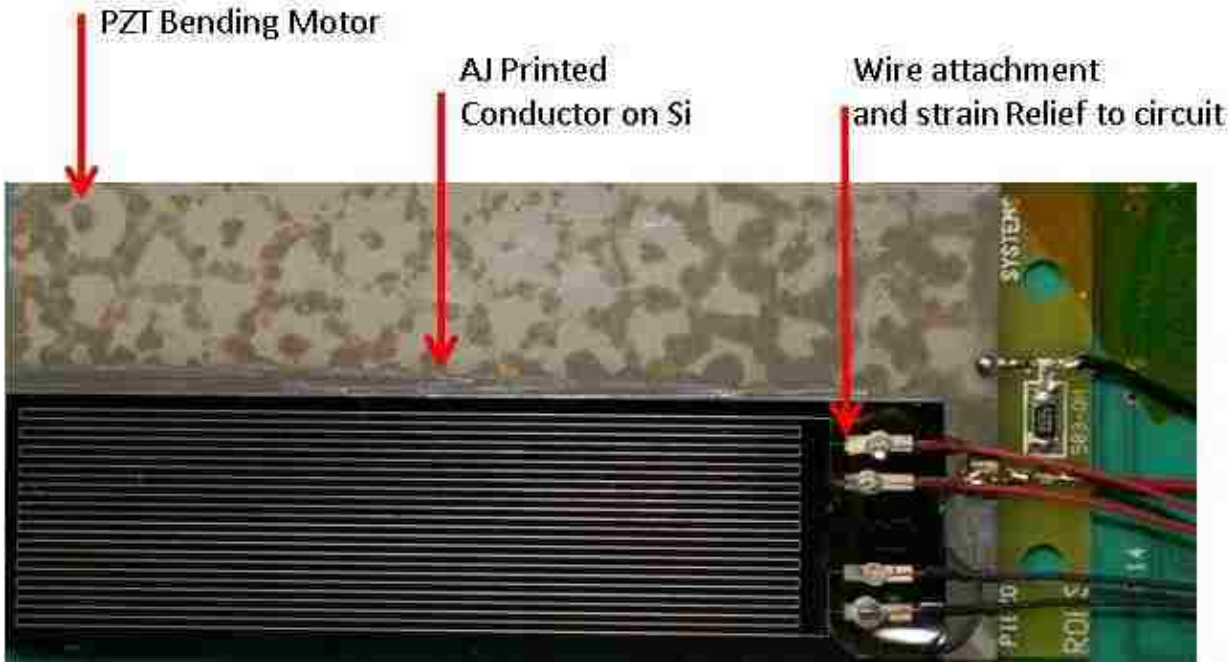

Figure 11: Printed and fully assembled evaluation circuit. Note four wire resistance measurement junction utilizing a fixed current input

The experimental set up allowed for the resistance measurement of four samples at a time. Prior to conducting aging studies at temperatures ranging between 20-55 ˚C, it was necessary to characterize the thermal coefficient or resistance (TCR) for the Aerosol Jet printed conductors in order to determine how much change in resistivity could be expected purely from temperature based effects. Four samples were placed into an oven and the temperature gradually increased from 17 ˚C to 55˚C. Changes in sample resistance as a function of temperature were logged for analysis. A Matlab script was written to calculate the TCR for the printed samples and is presented in Appendix 1. The TCR for each of four samples was calculated using Equation 2:

$$\text{Equation 2: } R = R_{ref}((1 + \alpha(T - T_{ref}))$$

where R_{ref} is the resistance of the sample at reference temperature T_{ref}, and α the coefficient of thermal resistance at a given temperature T.

A least squares fit of the data revealed a linear relationship between sample resistance and temperature change over the thermal region of interest, Figure 12. The experiment revealed values of α which ranged between 0.000734 and 0.00108 per degree Celsius, below the TCR for bulk silver at $\alpha = 0.003819$. With this information, it was surmised that any change in sample resistivity as a function of temperature would be small and as such could be neglected as a source of large changes in conductor resistivity.

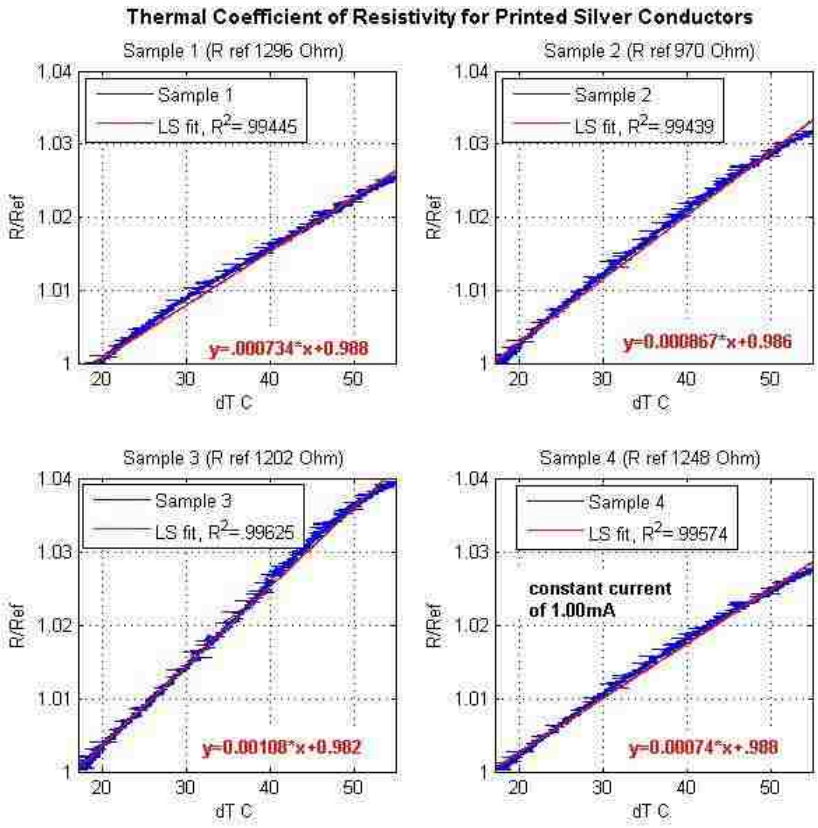

Figure 12: Temperature coefficient of resistivity curves for Silver Aerosol jet printed conductors

.

In the actual fatigue tests, three samples were subjected to dynamic fatigue testing while one sample was used as a static control. 1 mA of current was sourced through each of the printed and sintered conductors. Resistance was calculated as a function of the

voltage dropped across the sample at the drive current and logged electronically for later analysis. A maximum strain of 0.0008% (Appendix 2) was applied to the three evaluation coupons at frequencies ranging between 5 -50 Hz and at temperatures between 17 ˚C and 55˚C. Resistivity was defined as the product of cross-sectional area *A* and sample resistance *R* divided by conductor length *L*, and has resultant units Ω·cm, Equation 3.

$$\textbf{Equation 3: } \boldsymbol{\rho = \frac{AR}{L}}$$

Sample cross-sectional areas were obtained using scanning contact profilometry (Dektak, Plainview, NY). Figure 13 shows a sample set of data from the profilometer studies, and a Matlab script written to calculate and plot resistivity as a function of cycle count using this data (Appendix 3).

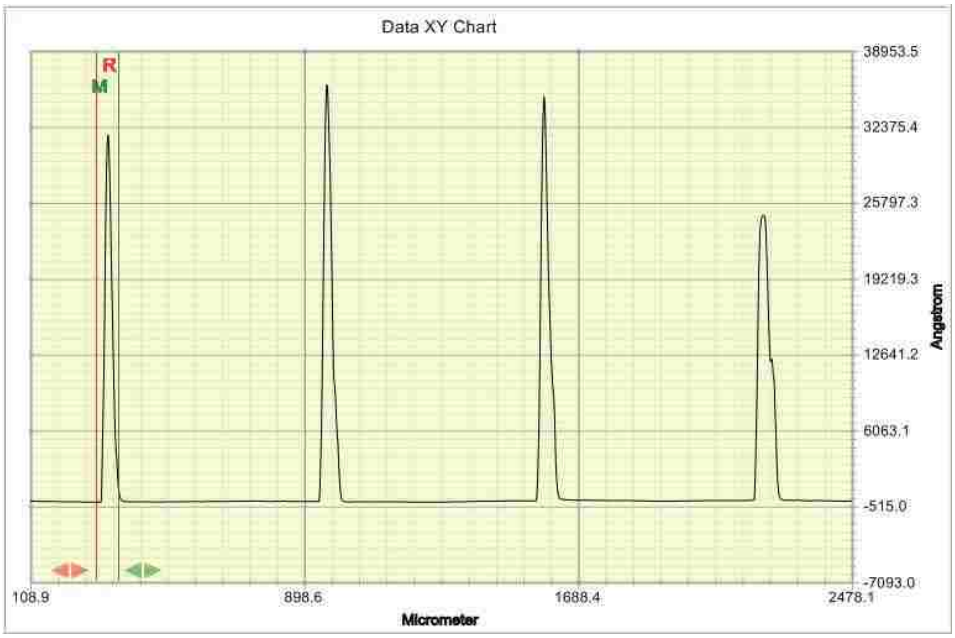

Figure 13: Contact profilometry of a sintered AJ printed silver nanoparticle deposition, 95 square microns (55°C sample 1)

Results:

The first attempt to evaluate printed conductor fatigue was performed at a rate of 5 Hz on 550 micron thick $[\bar{1}10]$ silicon with an applied strain of 0.0008%. A single sample was evaluated at room temperature and resulted in an appreciable 77.7% resistivity change over the course of approximately eight million cycles as seen in Figure 14.

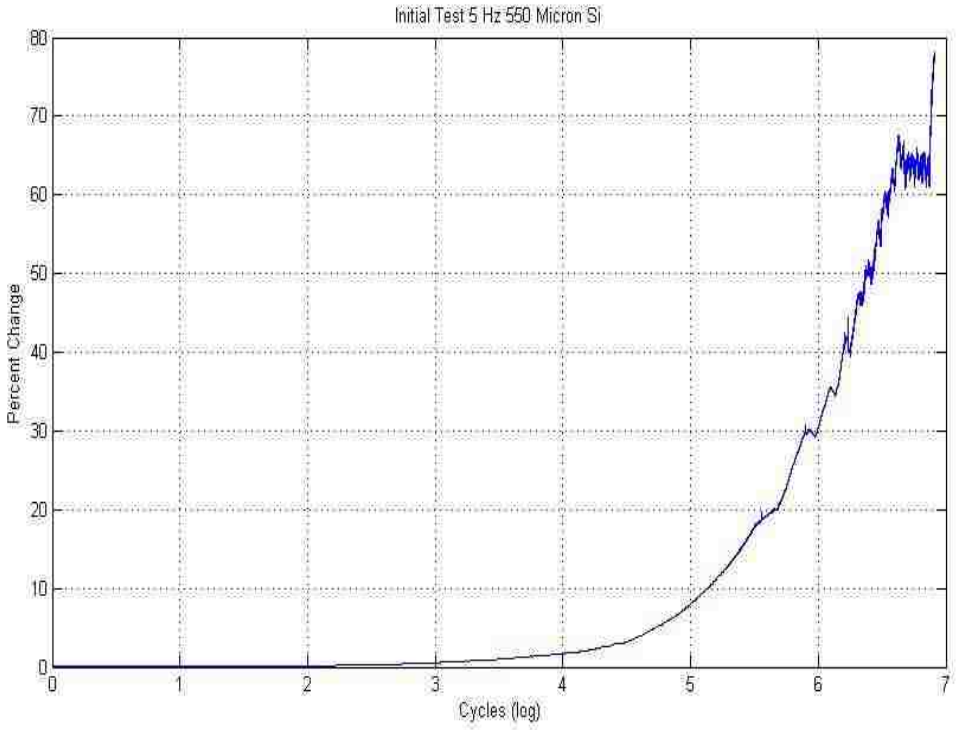

Figure 14: Conductor fatigue manifest by a resistivity increase in the initial proof of concept tests.

A change in sample resistivity from 1.799 x 10^{-6} Ω·cm to 3.124 x 10^{-6} Ω·cm suggested that the fatigue mechanism hypothesized to occur with the application of strain did in fact take place. This preliminary test provided a reasonable belief that the testing

methodology, materials selection, and analysis techniques were sound and that further experimentation was warranted.

In an effort to minimize substrate effects in a printed conductor, samples were deposited on 25 micron thick silicon and subsequently evaluated at room temperature. The full analysis of the effect on substrate thickness as it pertains to strain in the printed sample is presented in Appendix 2, but the thinning of the substrate resulted in a reduction of the strain in the printed sample to 0.000059% from 0.00081%. . At this time the decision to increase the cycle rate from 5 Hz to 50 Hz was made in order to reduce the time per sample in test. At 5 Hz, it takes approximately 19 days to obtain 8 million cycles The rationale behind this decision was to reduce data acquisition testing times from 19 days to just under two days while maintaining a high cycle count test. After approximately eight million cycles at 50 Hz and 0.000059% strain, a much smaller percent change was observed as shown table 1 and Figure 15. The percent change sample resistivity was calculated using equation 4:

$$\text{Equation 4: } \%\ Change = \frac{\rho - \rho_o}{\rho_o} \times 100$$

where ρ and ρ_o represent the resistivity and initial resistivity of a sample.

Sample	Maximum Percent Change
1	0.75
2	0.89
3	0.87
4 (static control)	1.78

Table 1: Percent change in conductor resistivity after cycling at room temperature and 50 Hz, 25 micron thick silicon

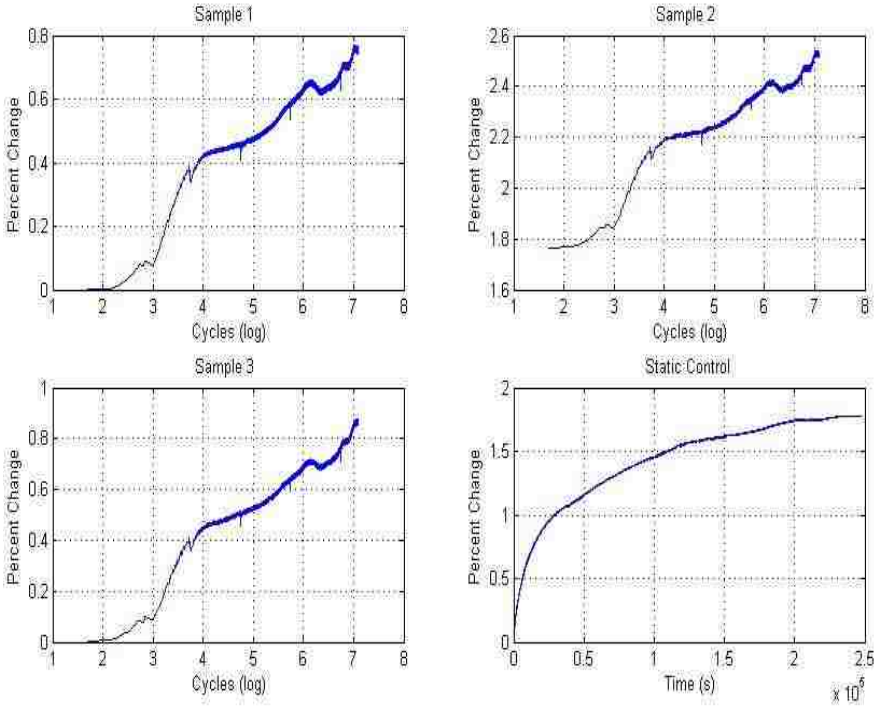

Figure 15: Resistivity increase for samples 1-3 cycled at 50Hz and at room temperature.

The lack of agreement between the first two fatigue tests was cause for concern. Further research revealed that fatigue mechanisms can be rate dependent.[24,25] Additionally, suspected ink quality issues warranted SEM analysis of the samples evaluated at 50 Hz. Figure 16 depicts the presence of defects in the printed and sintered silver nanoparticle conductors. A top down view revealed micron sized angular structures which were not immediately identifiable. Recall from the background discussion that samples printed in the presence of surface defects had very anomalous behaviors, due to the fact that the defects often acted as stress concentrators or otherwise perturbed the test. These large defects in the printed samples were not initially observed in earlier printed samples and testing, and warranted further analysis.

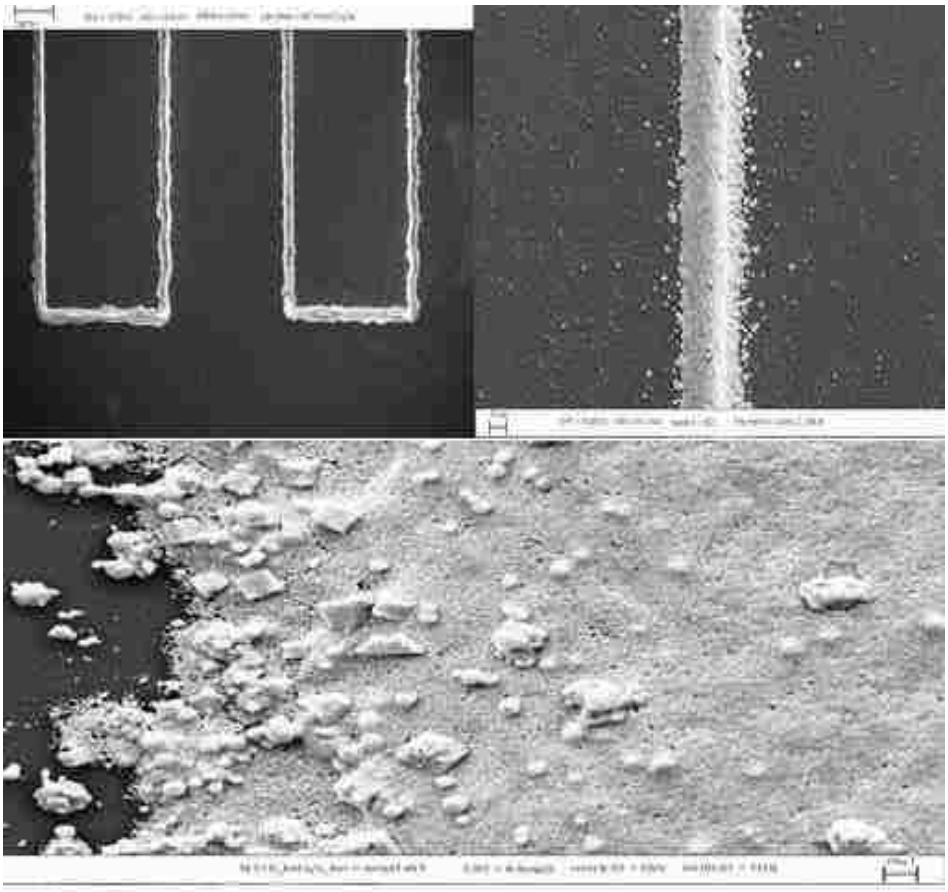

Figure 16: SEM of printed conductors revealing the presence of a suspected contaminant

Further analysis with Energy Dispersive X-Ray Spectroscopy (EDS), Figure 17, revealed the presence of chloride, a contamination suggestive of quality control, reliability, and repeatability issues with the manufacture of the selected ink. The interaction, if any, of this element with the printed conductor was unknown and a determination of whether the contaminant was causal in the reduced resistivity changes could not be made. Certainly, however, the existing of a second phase in the printed material that is structurally much different than the sintered silver material can be expected to have a large effect on mechanical behavior, as these inclusions would act effectively as stress concentrators or discontinuous inclusions within the printed matrix.

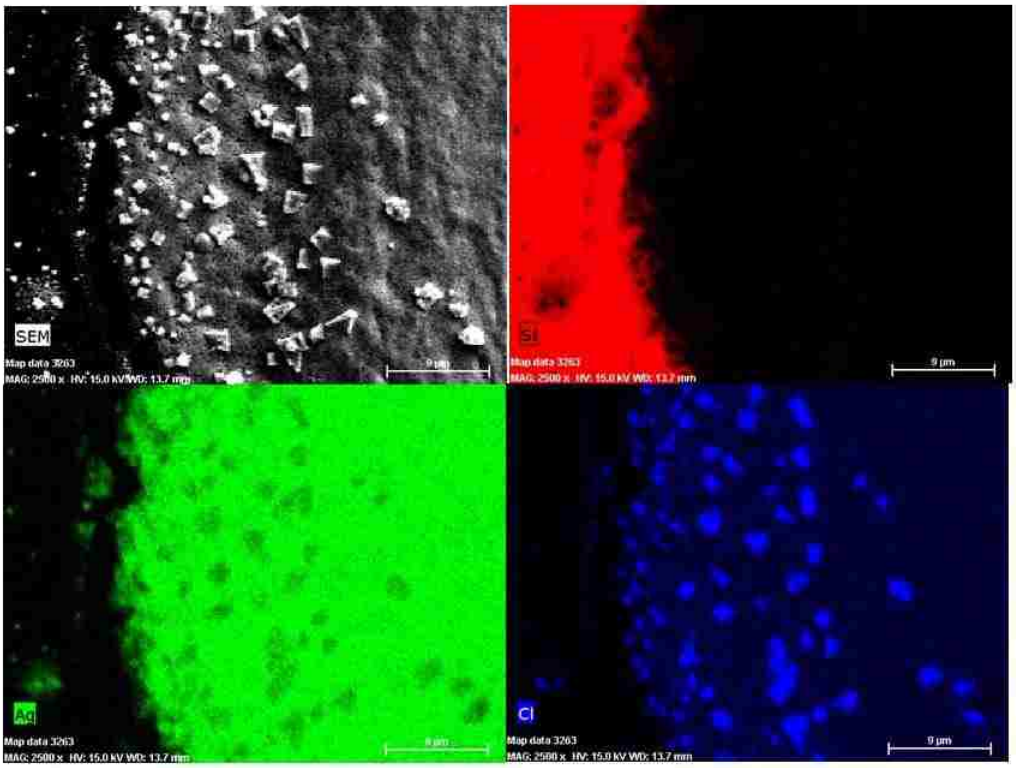

Figure 17: EDS revealing the presence of chloride contamination in the selected ink.

The choice of a 25 micron thick silicon substrate proved extremely difficult to handle and process and was subsequently abandoned in favor of the thicker substrate. This decision was further warranted as once calculated, the strain induced in the ultra-thin silicon proved to be less than the strain induced in the thick silicon substrates, Appendix 2. 550 micron thick silicon was used for the remainder of all tests. As per the ink supplier's recommendation, an attempt to remove the cubic structures through filtration of the ink using a 0.2 micron syringe filter was made. While SEM verified the absence of the micron sized cubic structures initially observed in post processing, Figure 18, EDS still indicated the presence of nanometer sized cubic chloride structures.

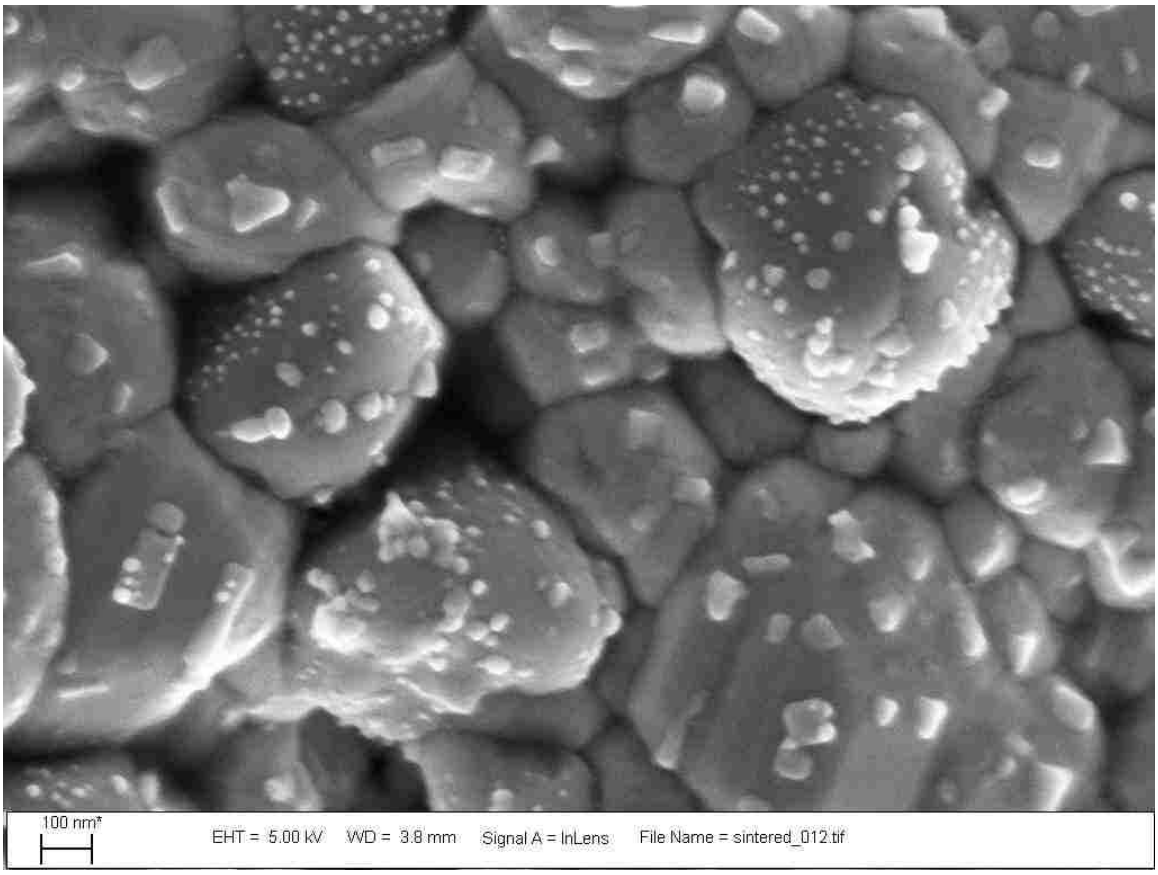

Figure 18: SEM verifying the removal of micron sized cubic contaminants, but still indicating nanometer sized chloride feature

The chlorides presence in the printed materials was not observed in the cross section and appeared to be limited to the surface of the depositions, Appendix 4. Additionally, an EDS spectral comparison between a sintered (red line) an un-sintered (blue line) sample show a change in peak location and intensity for chloride, Figure 19. While filtration may have removed a portion of the crystalline contaminant present in the ink, it is possible that the evolution of cubic chloride structures is the result of thermal heating and subsequent precipitation of the chloride present in the ink system.

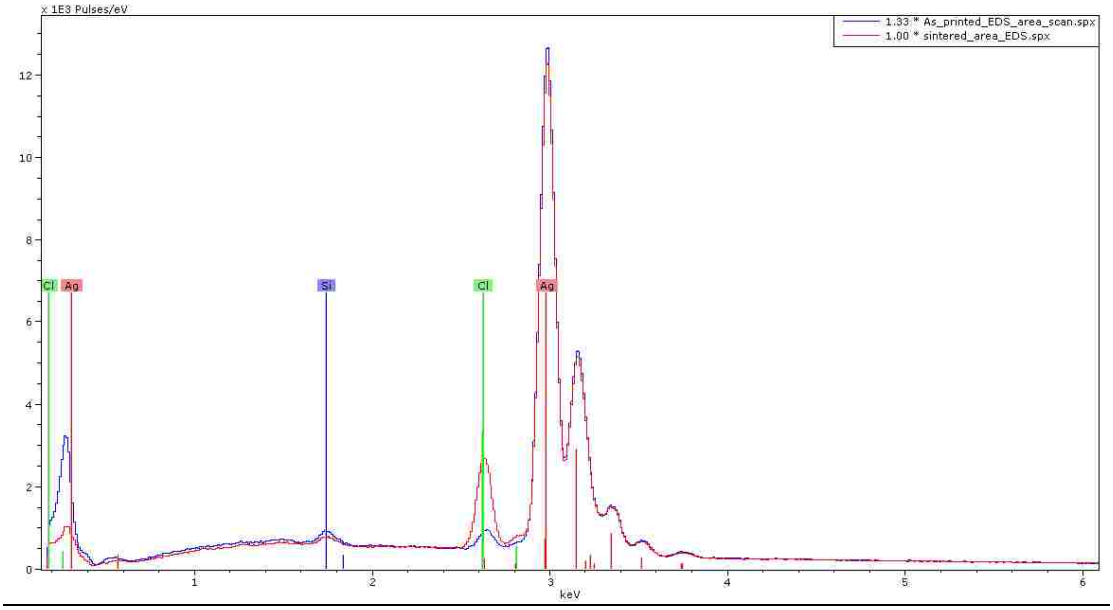

Figure 19: EDS spectral overlay of a sintered (red line) and un-sintered (blue line) sample. Note the shift in location and intensity of the chloride signal.

All subsequent tests were conducted at 5Hz and on 550 micron thick substrates, which matched what was used in the original test sample. Once samples had been prepared and fixtured for testing, the preliminary experiment was repeated. At room temperature, approximately 17˚C- 22˚C, three samples were subjected to approximately 8 million cycles at 0.0008% strain while one sample acted as the groups' static control for the group. Once again the same magnitude change in resistivity increase which was initially seen was not observed. Table 2 tabulates the samples maximum percent resistivity increase while figure 20 shows the response through cyclic loading.

Sample	Maximum Percent Change
1	1.81
2	3.15
3	3.94
4 (static control)	1.79

Table 2: Percent change in conductor resistivity after cycling at room temperature (approximately 22˚C) and 5 Hz, 550 Silicon

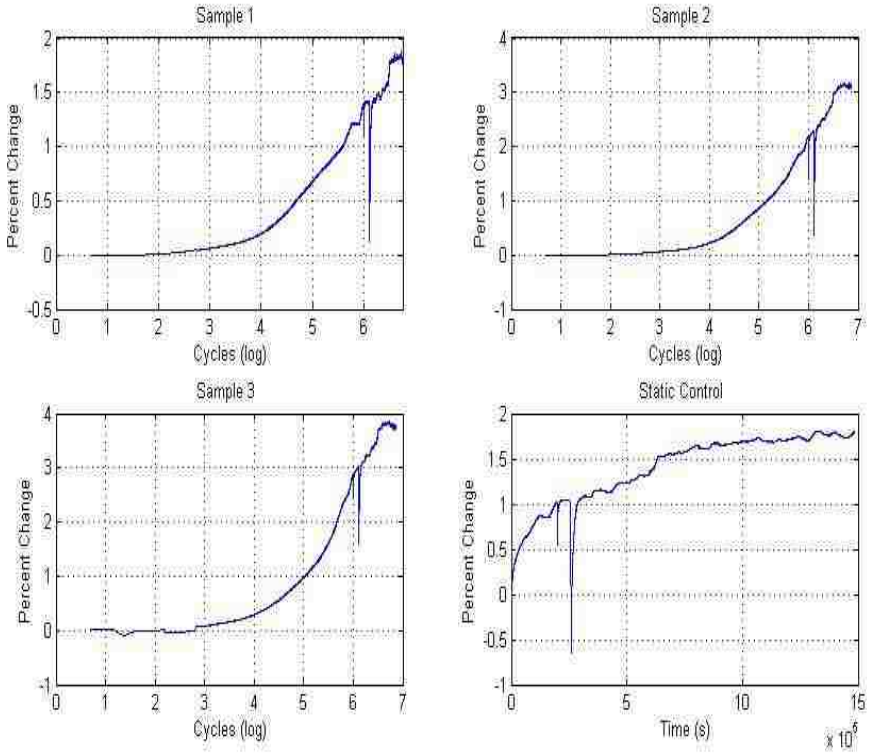

Figure 20: Resistivity increase for samples 1-3 cycled at 5Hz and at room temperature.

Fatigue evaluation of printed conductors was subsequently conducted at 35 ˚C. As with the previous experiment, samples were subject to 0.0008% strain.

After approximately eight million cycles, a uniform percent increase in sample resistivity was observed across the printed test coupons, table 3 and figure 21.

Sample	Maximum Percent Change
1	1.70
2	1.53
3	1.47
4 (static control)	2.11

Table 3: Percent change in conductor resistivity after cycling at 35 ˚C and 5 Hz, 550 Silicon

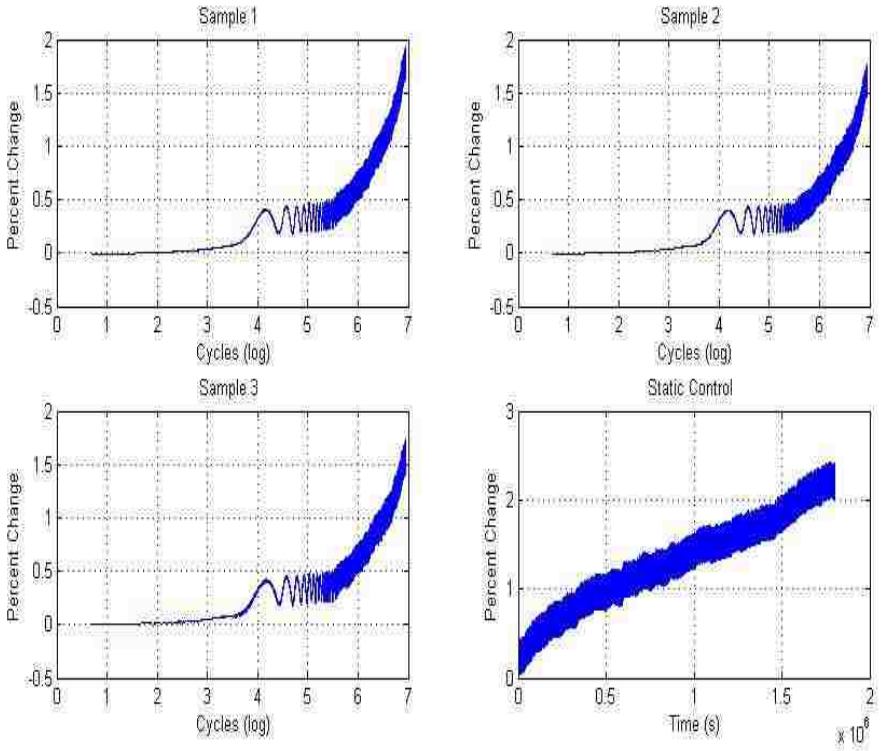

Figure 21: Resistivity increase for samples 1-3 cycled at 5Hz and 35˚C.

With these new samples and with the new, filtered ink, these tests data showed a change, but it was much less than what was observed during the initial experiment. In an effort to exaggerate the fatigue mechanism shown in the original experiment and believed to occur based on the literature review, samples were evaluated at 55 ˚C. Using the methodology previously described, three samples were subjected to 0.0008% strain and one sample implemented as a group control. The samples were cycled at 5 Hz to

approximately 8 million cycles. The results of this experiment once again showed a minimal change in two of the cycled samples. However, one of the samples evaluated exhibited a sharp increase in resistivity after approximately 1 million cycles. Table 4 tabulates the maximum percent resistivity changes in the samples cycled at 5 Hz and 55˚C. Figure 22 reveals a variable response with as much as a 60% change in resistivity in sample three as a possible result of mechanical aging induced by cyclic loading.

Sample	Maximum Percent Change
1	4.45
2	4.61
3	68
4 (static control)	4.2

Table 4: Percent change in conductor resistivity after cycling at 55˚C and 5 Hz, 550 Silicon

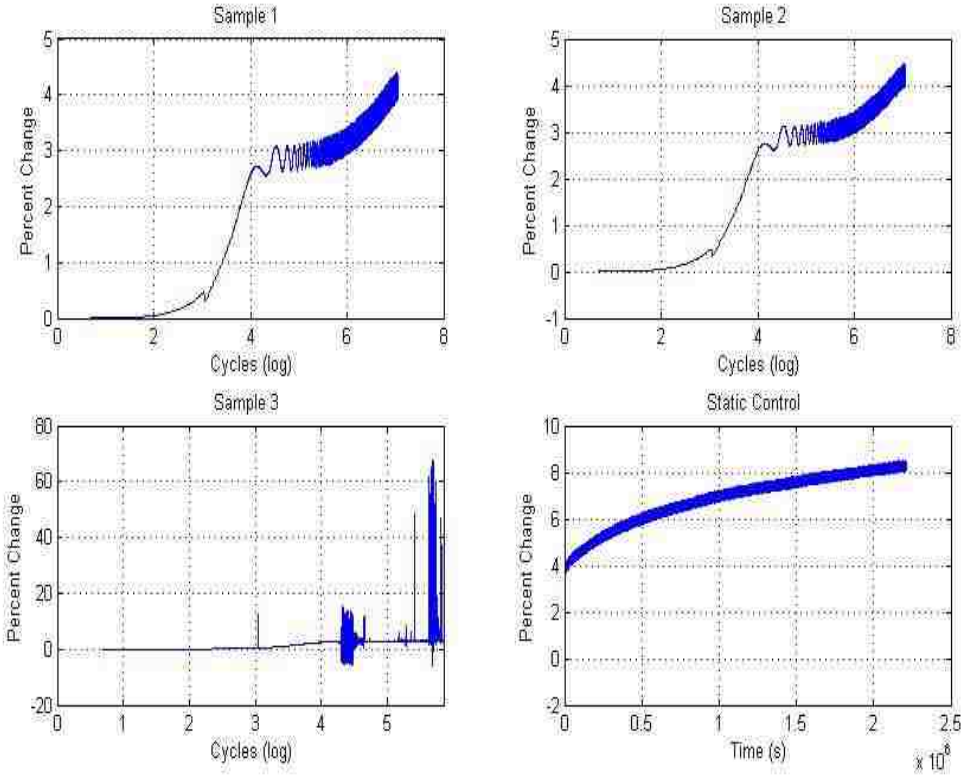

Figure 22: Resistivity increase for samples 1-3 cycled at 5Hz and at 55° C Note the inconsistent behavior from sample 3.

The hypothesized explanation for the sharp rise in sample three's resistivity increase was the formation of micro cracks induced by mechanical fatigue. This hypothesis was tested through the use of thermally-induced voltage alteration (TIVA) of sample 3. TIVA is an analysis technique in which constant current is sourced through the sample and heat applied to a conductor via a laser. A voltage change in the conductor as a result of applied heat generates a local electromagnetic field (EMF) which can be optically imaged.[26] As the silver conductor printed atop the silicon substrate generates an EMF and resistance change at a different rate than the underling substrate for a given thermal input, any break in the conductor would be evidenced by an absence of an EMF at a point, presumably a break in the printed conductor. The use of TIVA in this

experiment was perused as a qualitative method for defect location and to minimize SEM analysis of the 1250 millimeter long conductor. However, a definitive break in the conductor was not observed. The TIVA image below, figure 23, shows a contrasting EMF gradient along the printed conductor.

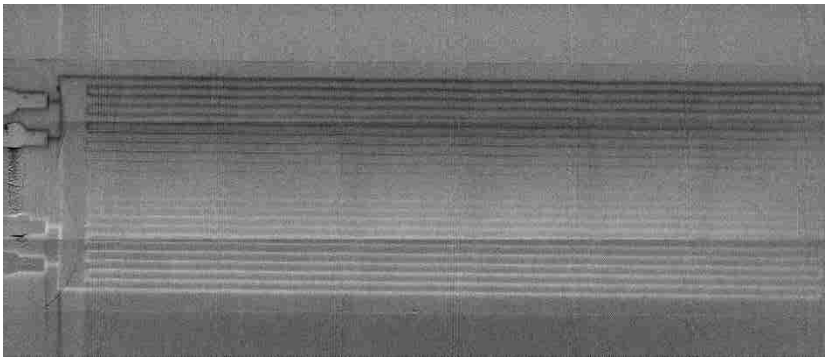

Figure 23: TIVA image showing constant EMF gradient from lower left to upper left of the printed conductor.

The smooth and continuous resistance change with the application of laser energy over the sample failed to isolate the suspected defects location. Had the technique been successful in defect location, the contrasting gradient along the sample would have been replaced with a definitive light-to-dark transition in the detected EMF at the specific location of the break.

The sample was further subjected to rigorous SEM analysis which was successful in isolating a single major defect believed responsible for the erratic behavior, Figure 24. At the site of a large inclusion, a fracture in the printed conductor was observed. Assuming the region of the conductor obscured by the inclusion was discontinuous, a three micron wide section of printed conductor is all that remained post cycling.

This significant reduction is cross sectional area is believed to account for the dramatic increase in sample resistivity and erratic behavior in resistance measurement during fatigue testing of sample 3.

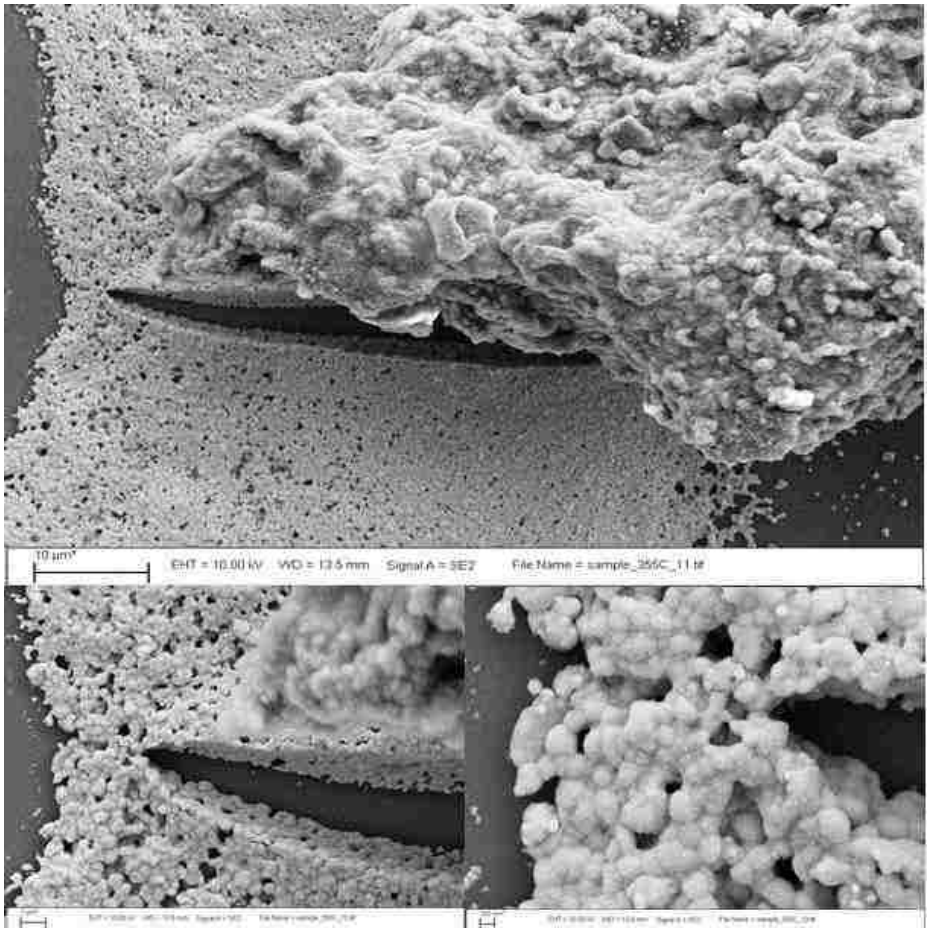

Figure 24: SEM of defect responsible for resistivity changes in sample 3, 55°C test.

After the thorough evaluation and analysis of printed conductors at various temperatures and rates of strain, a concern regarding the amount of current applied to the printed samples arose. The four point resistivity measurement preformed during the testing of the devices utilized 1 mA of applied current. However, based upon estimations of current densities in actual conductor lines used in photovoltaic systems, currents as high as 22mA may exist in collector grid lines in operational photovoltaics. This

estimation is based on a collector grid spacing of 2 millimeters, a 7.13 Amp production per photovoltaic cell, and the presence of two bus lines which carry current from the cell to the point of use. Dividing the current production of the photovoltaic cell by the number of collector lines present, the current carrying capacity of each line can be determined. With 2 millimeter spacing and the presence of 312 individual collector lines per 156mm x 156mm cell, it was possible to arrive at the 22 mA estimation. Appendix 5 further details this analysis.

To evaluate a series of printed devices at higher current density, a test was performed in which 20 mA of applied current was sourced through three printed samples. The experimental set up was modified to include three current sourcing units. The samples were subjected to 0.0008% strain and cycled at 5 Hz and 55 ˚C to approximately six million cycles. A failure of the data collection system prevented the evaluation to eight million cycles as planned. It was hypothesized that the increased current load through the samples would have a negligible effect as thermal breakdown of the printed conductors would be inhibited by heat transfer of the resultant thermal energy to the silicon substrate. Table 5 and figure 25 show the results of the final test.

Sample	Maximum Percent Change
1	1.36
2	1.48
3	1.27
4 (static control)	2.64

Table 5: Percent change in conductor resistivity after cycling under 20 mA, 55˚C and at 5 Hz, 550 Silicon

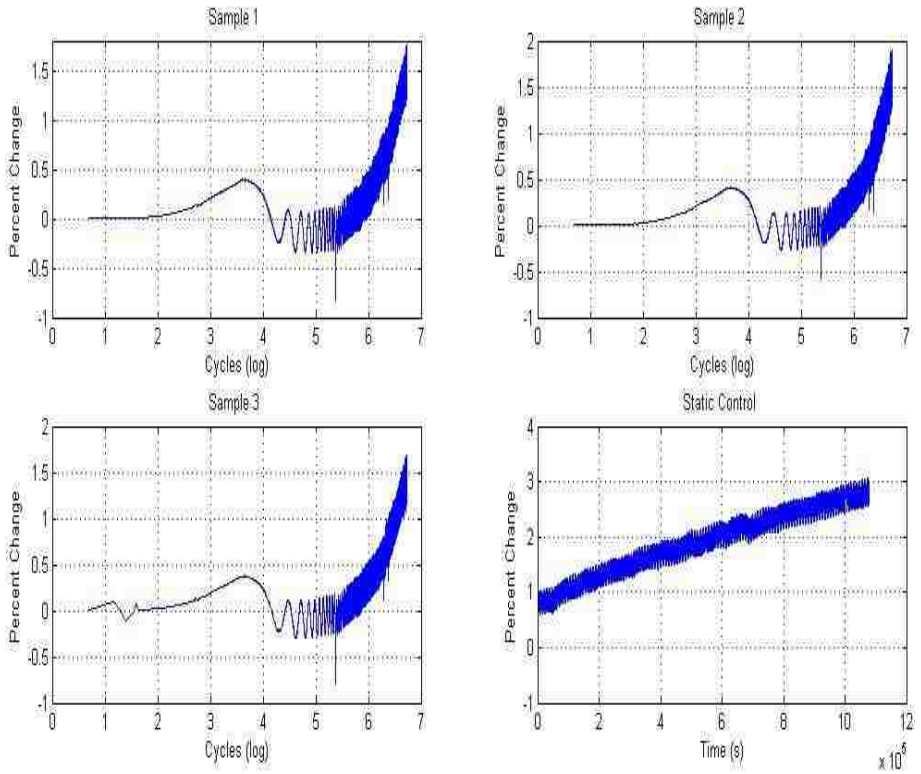

Figure 25: Resistivity increase for samples 1-3 cycled under 20 mA, 5Hz and at 55° C, 550 micron silicon. Cross sectional sample areas were estimated based on measured samples from all other experiments.

As expected, the application of increased current density through the printed conductor on silicon was inconsequential. As was observed in the previous sample set evaluated at 55°C, an indication of fatigue induced crack formation was not detected. However, the nominal percent change in resistivity as compared to other samples evaluated at 55 °C was lower. A determination as to whether or not the application of an increased current density is responsible for this observed result cannot be ascertained at this time.

Discussion and Conclusion:

The evaluation of AJ printed silver nanoparticle conductors revealed the presence of an aging mechanism with increasing cycle count but cannot be solely attributed to an applied strain. Attempts to prepare specimens on ultra-thin 25 micron silicon proved to be a poor choice for several reasons. The handling and manipulation of the substrates was extremely difficult and resulted in excess breakage which could not be supported by the inventory of wafers on hand. More importantly, the calculated rate of strain to the silicon for the maximum deflection permitted by the experimental set up was demonstrated to be less than what was induced in the thicker 550 micron substrates.

Maximum percent changes in the three samples evaluated at 50 Hz and on ultra-thin silicon ranged from 0.075% to 1.78%. The static control sample experienced a 2.52 % change in resistivity over the duration of the experiment, supportive of an aging mechanism not directly studied. This is shown in Figure 25 which relates the percent change of the three dynamically strained samples to the static control for the experimental set.

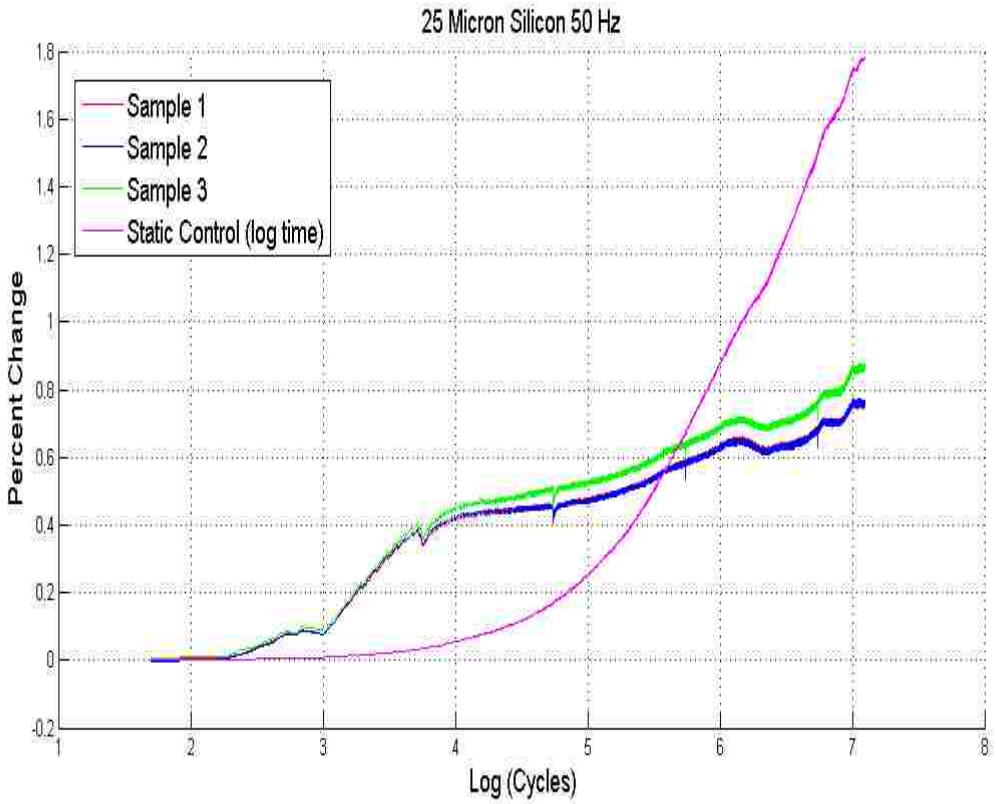

Figure 26: Percent resistivity increase for the 50 Hz, room temperature experiment. Note the nearly identical changes between sample's 1 and 2 as a result of equal initial resistance.

SEM and EDS analysis of theses samples revealed the presence of cubic chloride structures in the ink but did not reveal the presence of any crack or defect formation, Figures 27. To remove the chloride which was believed to be a contamination of the ink, filtration through a 0.02 micron syringe filter was performed. While this was successful in the elimination of micron sized contaminants, 100-200 nanometer contaminants were still present in the printed and sintered materials, or were precipitated out during the drying and curing processes.

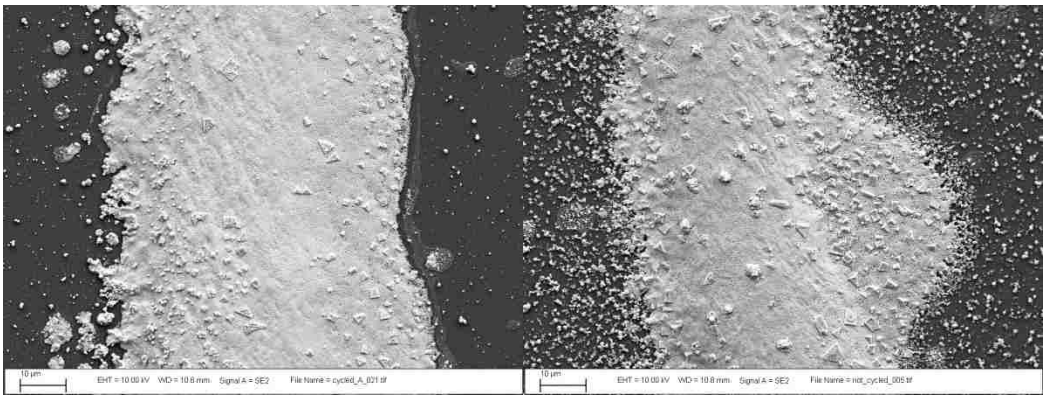

Figure 27: Right, cycled and strained sample. Left, static sample. Note lack of crack formation or surface defects in both images.

Specimens evaluated at room temperature, 5 Hz, and on 550 micron thick silicon exhibited percent changes in resistivity ranging from 1.81% to 3.94%, far below the 77% change observed in the initial experiment. The resistivity of the static control sample was observed to change by 1.79%. This initially suggested that in the case of the samples evaluated at room temperature and on 550 micron silicon, an aging effect as the result of applied strain and increasing cycle count was present. However, the steadily increasing resistivity of the static sample is indicative of a yet unidentified aging mechanism such as oxidation of the printed samples. Figure 28 below indicates an equally increasing rate of resistivity across the entire set. Consequently, it does not appear as if aging as a result of applied strain is solely responsible for the increase in sample resistivity for this data set.

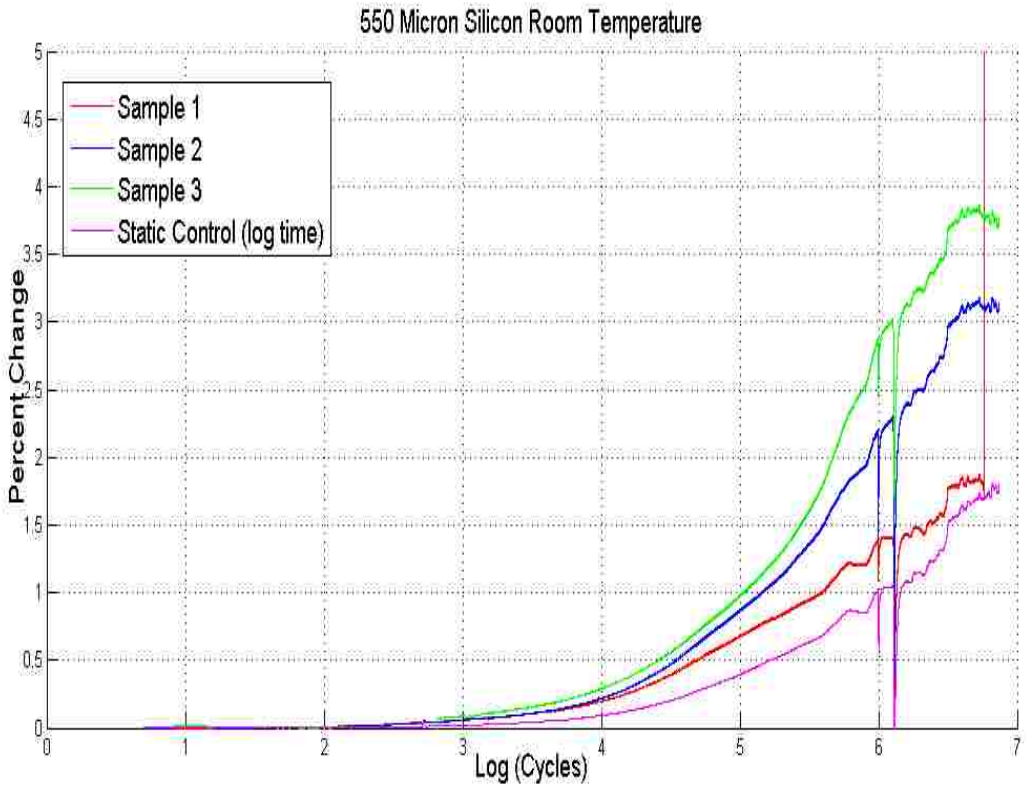

Figure 28: Percent resistivity increase for the 5 Hz, room temperature experiment.

Printed conductors evaluated at 35 ˚C exhibited similar behavior in that the rate of increasing resistivity in the strained samples was similar to that of the group control. However, the nominal percent change in the 35 ˚C sample set was unexpectedly lower than that of the samples evaluated at room temperature as shown by figure 29 below.

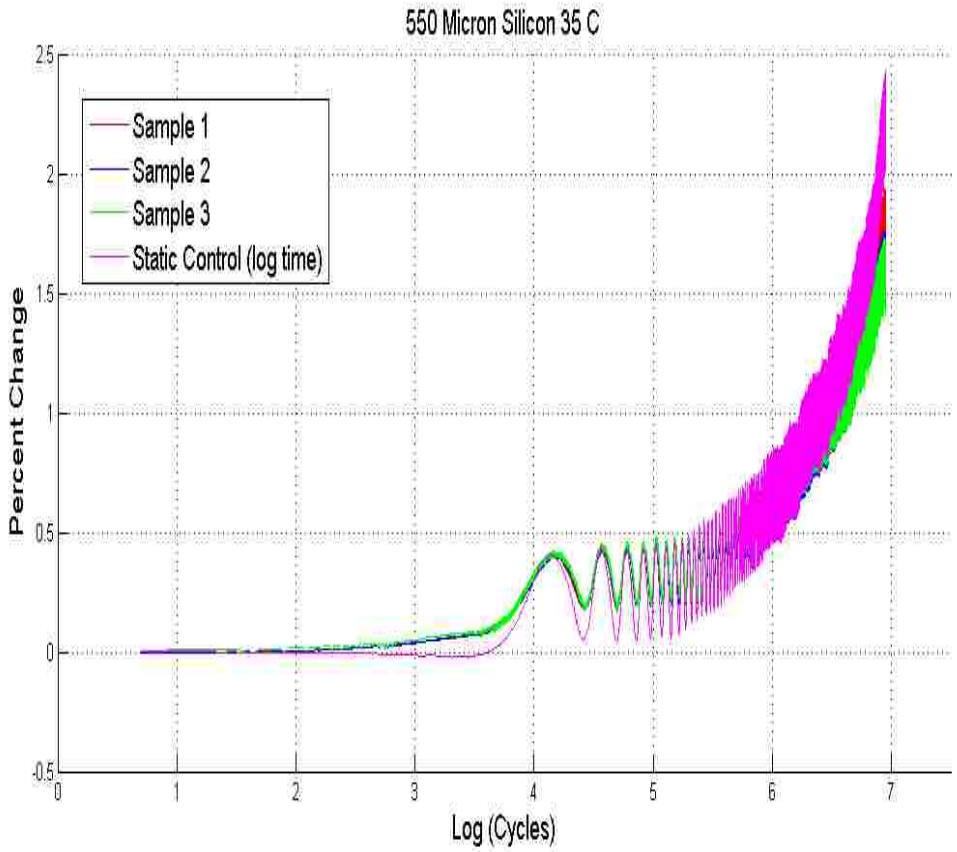

Figure 29: Percent resistivity increase for the 5 Hz, and 35 C sample set.

The samples evaluated at 55 ˚C and 5 Hz exhibited the highest percent change in resistivity. In particular, one sample was observed to increase dramatically and subsequently decrease in resistivity, figure 30. This behavior, believed to be the manifestation of crack formation was verified using SEM. A single defect which bisected most of the width of the printed line was observed and supported the hypothesized failure mechanism of fatigue-induced cracking in AJ printed conductors.

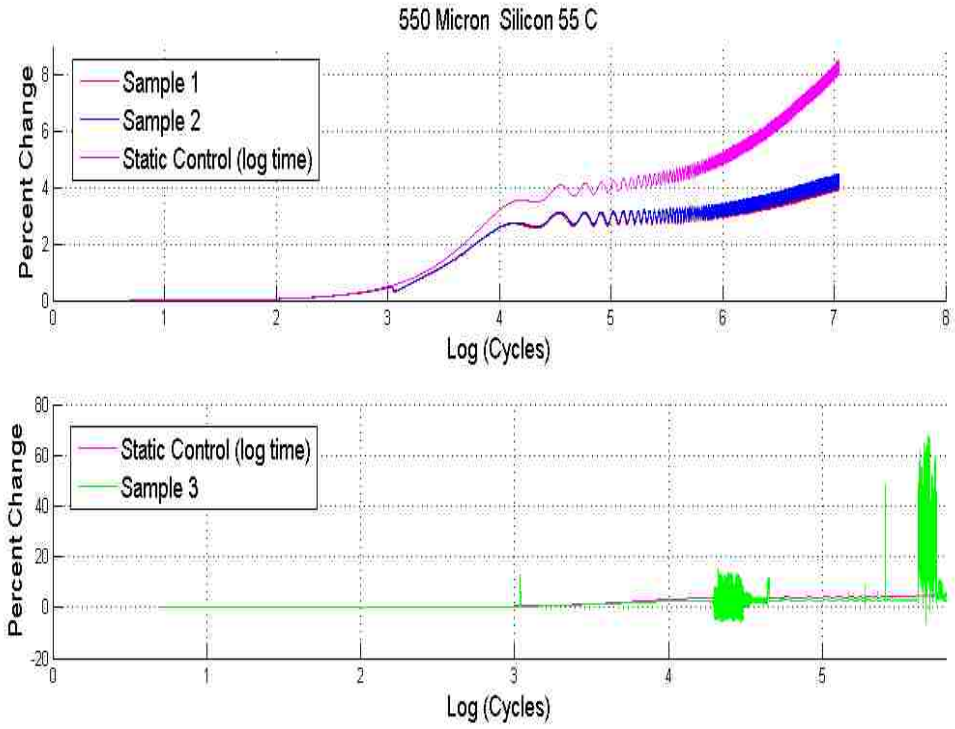

Figure 30: Percent resistivity increase for the 5 Hz, and 55˚C sample set. Note the increase and decrease in resistivity of sample three. SEM verified crack formation in sample 3 is believed responsible for the large changes in resistivity.

Samples evaluated at 20 mA current densities and 55°C did not show any unexpected behavior nor result in erratic resistivity measurements as a consequence of fatigue ageing. As the electrical measurements performed on theses samples did not indicate failure, these samples were not imaged using SEM. Figure 31 below shows a similar percent increase in resistivity as was observed in previous experiments.

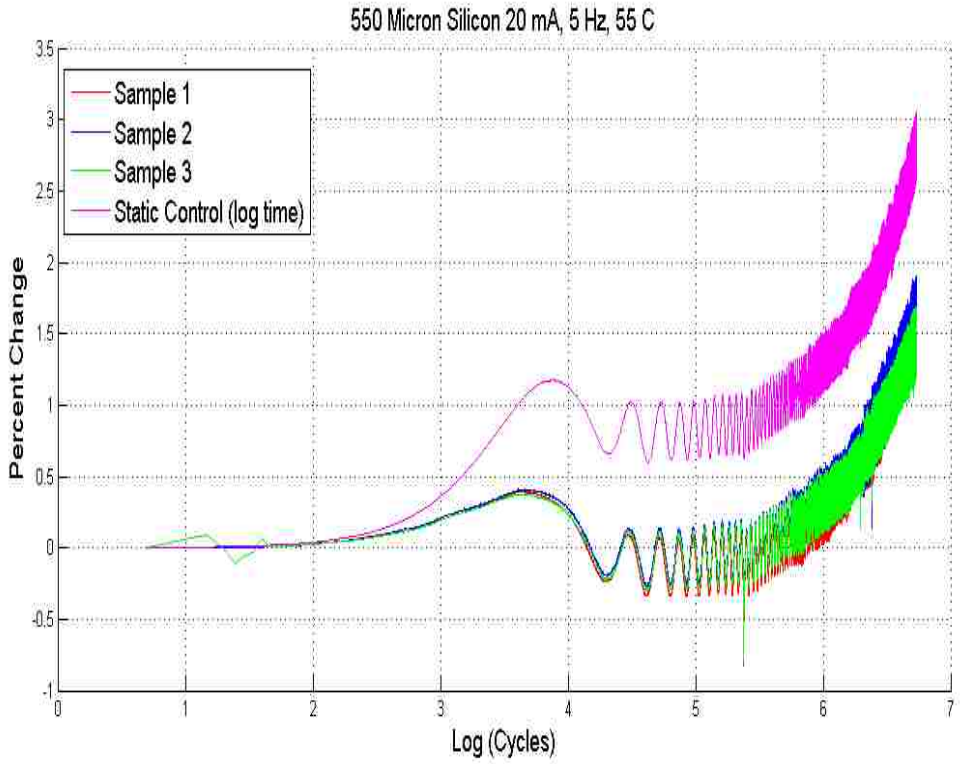

Figure 31: Percent resistivity increase for 20mA applied current, 5 Hz, and 55˚C sample set.

Periodic oscillations in the data for experiments conducted at elevated temperature were shown to be related to the heating profile of the oven over the course of several days. The most stable temperature profile occurred at room temperature and did not reveal an oscillatory resistivity change as a function of cycle count. The reality of this effect for experiments conducted at temperature is minor. In the case of the 35 ˚C experiment, a less than 0.5 percent change as a result of temperature instability resulted. The heating profile of the oven with respect to time is presented for completeness in figure 32 below.

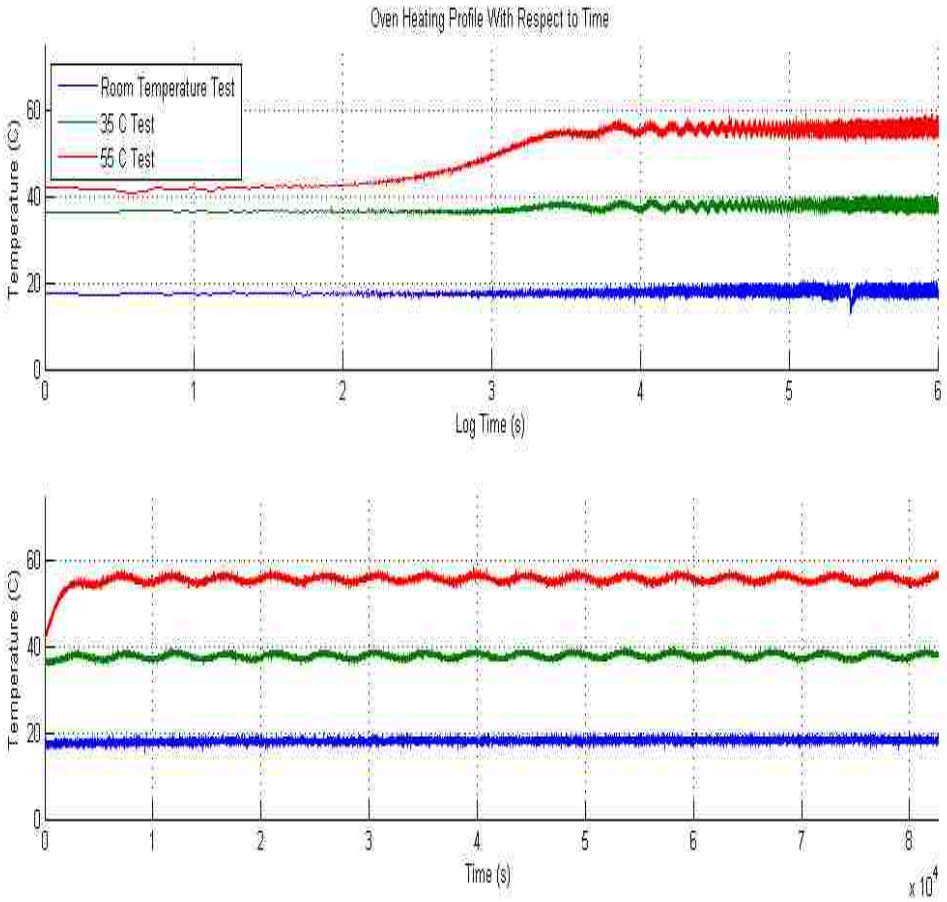

Figure 32: Oven heating profile explaining responsible for resistivity oscillation

Additional unidentified and uncontrollable process variation made the direct correlation between strain and cyclic loading difficult to determine. While the samples evaluated at 55˚C showed the largest increase in resistivity, samples tested at 35˚C showed a smaller change than did those evaluated at room temperature. Figure 33, which depicts a dramatic variance in cross-sectional profiles among cycled and un-cycled conductors, suggests an inability to precisely control the AJ deposition process. These samples, which were all printed at the same time and using the same aliquot of silver ink, exemplify a variable process which cannot be accounted for during fatigue testing. This

cross sectional variation is directly removed from the measurements through the use of resistivity calculations rather than resistance. However, the fact that this variation in line cross section occurs under nominally identical deposition conditions indicates that other processes may be occurring. Proposed process variations include ink aging or drying, variations in room temperature or environmental conditions, or agglomeration of the nanoparticles and are not being controlled during these experiments.

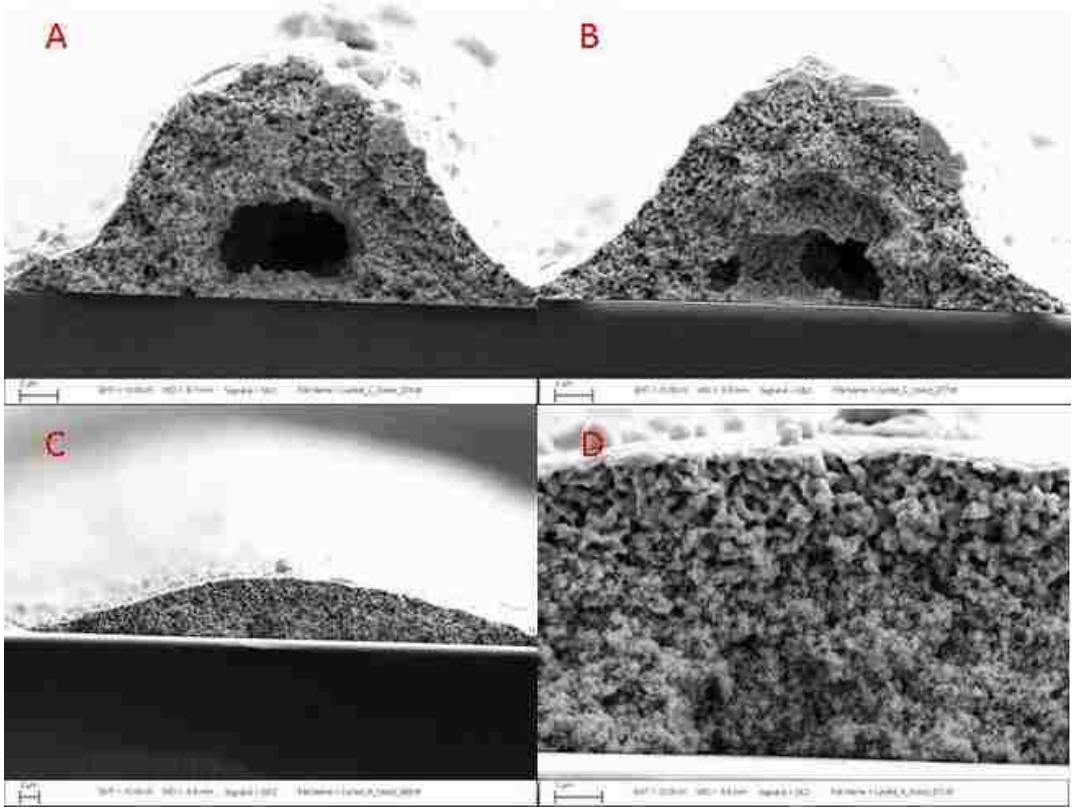

Figure 33: cross sectional variance in AJ printed materials. A, B, and C cycled, D static control.

An obvious source of printing variability may lie with the atomization of ink over time. The AJ method utilizes an ultrasonic nebulizer to generate a dense mist of nanoparticle material. Over the duration of the 15 minute per device printing process, the

1 mL ink reservoir is depleted by as much as 15%. Consequently, the ratio of solvent to solids dynamically changes and is a potential source of printing variability.

Further compounding the difficulty in fatigue evaluation was the duration required for collecting data. Including sample preparation, the evaluation of samples to eight million cycles at 5 Hz took approximately 22 days per series to complete. This experimentation bottleneck did not allow for the evaluation of additional ink chemistries, lower cycle rates, or similar experimental variables which may be of consequence to fatigue studies such as this one.

The initial experiment provided reasonable evidence that a maximum strain to the silicon of 0.0008% was sufficient to induce fatigue in a printed conductor. However, a static control was not implemented in this test and as such a comparative baseline to an un-cycled sample is unavailable. The experimental set up did not allow for the application of a higher strain rates which may be required to elicit the hypothesized fatigue mechanism in a more repeatable method. Larger PZT actuators, which would have allowed for higher applied strain rates, were not commercially available and did not manifest as a potential concern until after the conclusion of several full length tests.

The fatigue mechanism believed to occur as a consequence of applied strain in an AJ printed conductor was definitively observed once. Unfortunately, the initial experiments sample was destroyed in the removal of the sample form the bending actuator and never imaged. As an explanation to the increase in sample resistivity not accounted for by the hypothesized fatigue mechanism, it is proposed that oxidation of the printed silver nanoparticles may in part account for changes in printed conductor resistivity observed in this thesis. Qi et al. demonstrated that 15-55 nm silver nanoparticles deposited on silicon

via an electroless plating method experienced an increase in oxygen content over the duration of 12 days, figure 34[27].

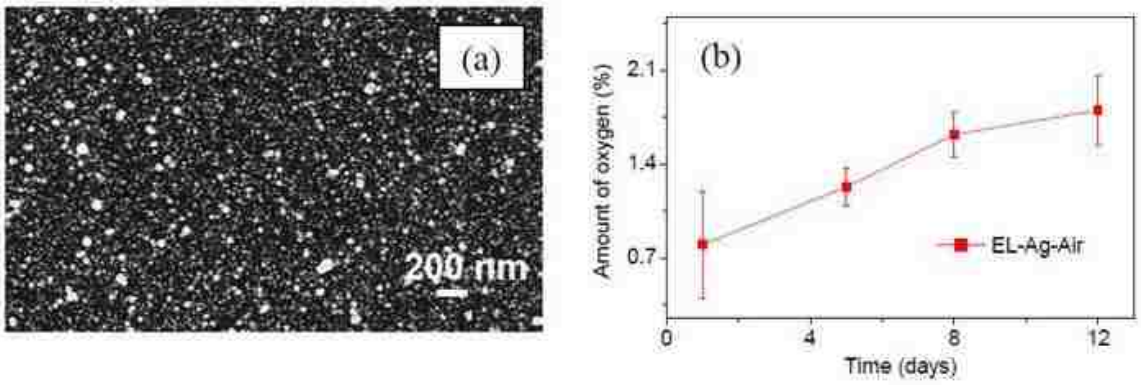

Figure 34: (a) SEM of 15-55 nm silver nanoparticles and (b) absorption of oxygen as observed with EDS[27]

This particle size range is similar to that used in the formulation of the silver ink chosen for AJ printing. It is well known that the oxidation of metals can result in an increase of conductor resistance and as such is a reasonable explanation for the experimental results observed in this thesis.

Closing:

The suitability of the AJ method for metallization of photovoltaic cells will largely be dependent on the stabilization of process variables and the minimization of printing variability during manufacture. Additionally, ink formulation and quality have an important role in the formation of low resistivity conductors suitable for current transfer over distances. To minimize the potential for oxidation in printed nanoparticle conductors, deposition and sintering equipment can be installed in inert and oxygen free environments. Subsequent encapsulation of the printed devices should minimize the potential for conductor degradation as a result of oxidation. Also, the elimination of large

inclusions during the printing process should be minimized as such features elevate the possibility of creating stress risers along otherwise stable conductor segments. Further investigation into the fatigue aging of printed nanoparticle conductors on silicon substrates is warranted as evidence of the hypothesized failure mechanism was observed only once. Additionally, the static control samples were not secured to piezoelectric actuators during the data collection phase of the tests. This variance in experimental technique as compared to the fatigued samples may have resulted in an inaccurate representation of the static control group's resistivity change with respect to time. The static control samples were not cantilevered in the experimental set up and were placed in direct contact with an aluminum block. While the assumption of an isothermal testing environment within the oven was made, it is possible that these samples experienced a slightly higher temperature than did the suspended cantilever samples. Also of importance is the realization that applied current densities experienced by the printed conductors may have been significantly higher than anticipated. As sintered nanoparticle material only approximate bulk metals and are comprised of a porous phases, the current sourced through a conductor may not have been transmitted evenly over the conductors cross section. This belief is supported by the measured reduction in coefficient of thermal resistance, and indicates that the electrical response of the AJ depositions behave differently than do bulk metals and as such deserves further investigation. Lastly, an identified shortfall of the experiment was the inability to induce higher rates of strain which may elicit a more reproducible and pronounced failure mechanism in the amorphous silver depositions.

Appendix 1: TCR calculation and plotting script

```
R1_ref=1296;  %sample resistance at initial condition of 17C
R2_ref=970;
R3_ref=1202;
R4_ref=1248;

subplot(2,2,1) %FOR SUBPLOT

plot(temp,Resistance1/R1_ref,'blue') %plots data

xlabel('dT C')
ylabel('R/Ref')
title('Sample 1 (R ref 1296 Ohm) ')
axis([17 38 1 1.04])
grid on
hold on
hleg1 = legend('Sample 1','LS fit, R^2=.99445');
plot(temp,y1fit,'red') %plots linear fit

    LS1=polyfit(temp,Resistance1/R1_ref,1); %sets up to find R^2 value
    y1fit=polyval(LS1,temp);
    y1resid=Resistance1/R1_ref-y1fit;
    SSresid1=sum(y1resid.^2);
    SStotal1=(length(Resistance1/R1_ref)-1)*var(Resistance1/R1_ref);
    rsq1=1-SSresid1/SStotal1 %R^2 value

subplot(2,2,2)
plot(temp,Resistance2/R2_ref)
xlabel('dT C')
ylabel('R/Ref')
LS2=polyfit(temp,Resistance2/R2_ref,1);
title('Sample 2 (R ref 970 Ohm) ')
axis([17 38 1 1.04])
grid on
hold on

hleg2 = legend('Sample 2','LS fit, R^2=.99439');
plot(temp,y2fit,'red')

    LS2=polyfit(temp,Resistance2/R2_ref,1);
    y2fit=polyval(LS2,temp);
    y2resid=Resistance2/R2_ref-y2fit;
    SSresid2=sum(y2resid.^2);
    SStotal2=(length(Resistance2/R2_ref)-1)*var(Resistance2/R2_ref);
```

```
    rsq2=1-SSresid2/SStotal2
%figure(3)
subplot(2,2,3)
plot(temp,Resistance3/R3_ref)
xlabel('dT C')
ylabel('R/Ref')
LS3=polyfit(temp,Resistance3/R3_ref,1);
title('Sample 3 (R ref 1202 Ohm) ')
axis([17 38 1 1.04])
grid on
hold on
hleg3 = legend('Sample 3','LS fit, R^2=.99625');
plot(temp,y3fit,'red')
LS3=polyfit(temp,Resistance3/R3_ref,1);
    y3fit=polyval(LS3,temp);
    y3resid=Resistance3/R3_ref-y3fit;
    SSresid3=sum(y3resid.^2);
    SStotal3=(length(Resistance3/R3_ref)-1)*var(Resistance3/R3_ref);
    rsq3=1-SSresid3/SStotal3
 subplot(2,2,4)
plot(temp,Resistance4/R4_ref)
xlabel('dT C')
ylabel('R/Ref')
title('Sample 4 (R ref 1248 Ohm) ')
LS4=polyfit(temp,Resistance4/R4_ref,1);
axis([17 38 1 1.04])
grid on
hold on

hleg4 = legend('Sample 4','LS fit, R^2=.99574');

plot(temp,y4fit,'red')

    LS4=polyfit(temp,Resistance4/R4_ref,1);
    y4fit=polyval(LS4,temp);
    y4resid=Resistance4/R4_ref-y4fit;
    SSresid4=sum(y4resid.^2);
    SStotal4=(length(Resistance4/R4_ref)-1)*var(Resistance4/R4_ref);
    rsq4=1-SSresid4/SStotal4
```

Appendix 2: Calculation of Strain

Strain was calculated by first defining the radius of curvature of the PZT and silicon system. The Keyence laser displacement sensor was fixtured to a micrometer and rigidly suspended above a sample. Working from the free end of the beam (as shown by figure 4) and without any actuation voltage applied to the bending motor, displacement readings were taken 500 microns in the direction of the fixed end. This process was repeated with a -90V bias applied to the bending motor and displacement measurements recorded. The differential in vertical displacement measurements between the biased and unbiased measurements resulted in a series of paired X-Z data points which were used to calculate the radius of curvature.

A MatLab Script was implemented, shown below, which applied a least squares curve fit to X-Z coordinate pairs and used to define the radius of a circle for the measured point data. Once the Radius of curvature had been determined, it was possible to directly calculate the Strain using the equations:

$$\frac{M}{I} = \frac{E}{R} = \frac{\sigma}{y} \; and \; specifically \; \frac{E}{R} = \frac{\sigma}{y}$$

And:

$$E = \frac{\sigma}{\varepsilon}$$

E is the modulus of elasticity, R, the calculated radius of curvature, σ the stress in the beam and y the distance from the free surface to the neutral axis. The strain, ε, can then be directly calculated. The table below tabulates the physical constants derived from and necessary to perform the above calculation.

	550 Micron Si	25 Micron Si
E (known)	$1.69 \times 10^{11}\ Pa$	$1.69 \times 10^{11}\ Pa$
R (measured)	35.16 meter	21.32 meter
y ½ sample thickness	.000275 meter	0.0000125 meter
σ Calculated	$1.32 \times 10^{6}\ Pa$	99,063 Pa
ε Calculated	0.0008%	0.000059%

Matlab script used to calculate the radius of a circle[28]

```
x=disp;
y=diff;
A = [x.^2+y.^2,x,y,ones(size(x))]; % Set up least squares problem
 [U,S,V] = svd(A,0); % Use economy version sing. value decompos.
 a = V(1,4); b = V(2,4); % Choose eigenvector from V
 c = V(3,4); d = V(4,4); % with smallest eigenvalue
 xc = -b/(2*a); yc = -c/(2*a); % Find center and radius of the
 r = sqrt(xc^2+yc^2-d/a); % circle, a*(x^2+y^2)+b*x+c*y+d=0
```

APPENDIX 3: Resistivity Calculations and Plotting Tools

The presentation of the analysis and plotting script has been presented in abridged form. Elements of the code not shown preform basic plotting functions not relevant to the data coverage of this thesis.

```
%**********************Data Plotting Tool*******************************
%   Import data file by selecting file import data from file menu.
%   Spec cs areas A1-A4 (cm^2) for Samples 1-4 in the command window
%   Spec sample length L
%   Execute script                                                Written By AWC
%************************************************************************
%conversion from time(s) to cycles and definition of log scales
time_50Hz;          %50 Hz test
cycles_50Hz=time_50Hz*50; %conversion to total number of cycles at 5 Hz
logcycle_50Hz=log10(cycles_50Hz); %conversion to base 10 log cycle
time_RT;          % Room temperature test
cycles_RT=time_RT*5;
logcycle_RT=log10(cycles_RT);
time_55C;          %55 C test
cycles_55C=time_55C*5;
logcycle_55C=log10(cycles_55C);
time_35C;          %35 C test
cycles_35C=time_35C*5;
logcycle_35C=log10(cycles_35C);
time_first_test;    %Initial test
cycles_first_test=time_first_test*5;
logcycle_first_test=log10(cycles_first_test);
 %**********************Area Definition*********************************
%sample_length =125cm for all samples;
L=125;   %Printed Sample length in cm
A1_50Hz=9.4e-7;     %Smallest sample cross sectional area 50 Hz test
A2_50Hz=8e-7;
A3_50Hz=9e-7;
A4_50Hz=9.1e-7;
A1_RT=9.0e-7;       %Smallest sample cross sectional area room temperature
A2_RT=10.9e-7;
A3_RT=9.8e-7;
A4_RT=9.1e-7;
A1_55C=9.8e-7;      %Smallest sample cross sectional area 55C test
A2_55C=13.8e-7;
A3_55C=9.8e-7;
A4_55C=9.1e-7;
A1_35C=9.5e-7;      %Smallest sample cross sectional area 35 C test
```

```
A2_35C=8.8e-7;
A3_35C=9.0e-7;
A4_35C=8.0e-7;
A_first_test=4.0e-7; % Smallest sample cross sectional area initial test
%**********50 Hz Definititions*********
%%resistivity calculated as:(Area*Resistance)/Length in cm and cm^2
Resistance1_50Hz;       Resistivity1_50Hz=(A1_50Hz*Resistance1_50Hz)/L;
%sample 1 resistivity
Hz_S1_initial=ones(247252,1)*1.9565e-6; %initial value matirx for percent
percent_50Hz_1=(((Resistivity1_50Hz-Hz_S1_initial)./Hz_S1_initial)*100);
Resistance2_50Hz;
Resistivity2_50Hz=(A2_50Hz*Resistance2_50Hz)/L;      %sample 2 resistivity
Hz_S2_initial=ones(247252,1)*1.9917e-6;
percent_50Hz_2=(((Resistivity2_50Hz-Hz_S2_initial)./Hz_S2_initial)*100);
Resistance3_50Hz;
Resistivity3_50Hz=(A3_50Hz*Resistance3_50Hz)/L;      %sample 3 resistivity
Hz_S3_initial=ones(247252,1)*2.2925e-06;
percent_50Hz_3=(((Resistivity3_50Hz-Hz_S3_initial)./Hz_S3_initial)*100);
StaticResistance_50Hz;
StaticResistivity_50Hz=(A4_50Hz*StaticResistance_50Hz)/L;%staticresistivity
Hz_S4_initial=ones(247252,1)*4.7291e-06;
percent_50Hz_4=(((StaticResistivity_50Hz-Hz_S4_initial)./Hz_S4_initial)*100);
%**********Room Temperature Definitions**********
Resistance1_RT;
Resistivity1_RT=(A1_RT*Resistance1_RT)/L;          %sample 1 resistivity
RT_S1_initial=ones(1481970,1)*1.891e-6;
percent_RT_S1=(((Resistivity1_RT-RT_S1_initial)./RT_S1_initial)*100);
Resistance2_RT;
Resistivity2_RT=(A2_RT*Resistance2_RT)/L;          %sample 2 resistivity
RT_S2_initial=ones(1481970,1)*2.0987e-6;
percent_RT_S2=(((Resistivity2_RT-RT_S2_initial)./RT_S2_initial)*100);
Resistance3_RT;
Resistivity3_RT=(A3_RT*Resistance3_RT)/L;          %sample 3 resistivity
RT_S3_initial=ones(1481970,1)*2.1640e-6;
percent_RT_S3=(((Resistivity3_RT-RT_S3_initial)./RT_S3_initial)*100);
StaticResistance_RT;
StaticResistivity_RT=(A4_RT*StaticResistance_RT)/L;  %static resistivity
RT_initial=ones(1481970,1)*2.1395e-6;
percent_RT_4=(((StaticResistivity_RT-RT_initial)./RT_initial)*100);
%**********55C Definitions**********
Resistance1_55C;
Resistivity1_55C=(A1_55C*Resistance1_55C)/L;       %sample 1 resistivity
S1_55C_initial=ones(2212241,1)*2.7478e-6;
percent_S155C=(((Resistivity1_55C-S1_55C_initial)./S1_55C_initial)*100);
Resistance2_55C;
Resistivity2_55C=(A2_55C*Resistance2_55C)/L;       %sample 2 resistivity
```

```
S2_55C_initial=ones(2212241,1)*4.9868e-6;
percent_S255C=(((Resistivity2_55C-S2_55C_initial)./S2_55C_initial)*100);
Resistance3_55C;
Resistivity3_55C=(A3_55C*Resistance3_55C)/L;       %sample 3 resistivity
S3_55C_initial=ones(2212241,1)*3.1749e-6;
percent_S355C=(((Resistivity3_55C-S3_55C_initial)./S3_55C_initial)*100);
StaticResistance_55C;
StaticResistivity_55C=(A4_55C*StaticResistance_55C)/L;%static resistivity
S4_55C_initial=ones(2212241,1)*6.2764e-6;
percent_S455C=(((StaticResistivity_55C-S4_55C_initial)./S4_55C_initial)*100);
%**************************35C Definitions*******************************
Resistance1_35C;
Resistivity1_35C=(A1_35C*Resistance1_35C)/L;       %sample 1 resistivity
S1_35C_initial=ones(1802865,1)*3.9028e-6;
percent_S135C=(((Resistivity1_35C-S1_35C_initial)./S1_35C_initial)*100);
Resistance2_35C;
Resistivity2_35C=(A2_35C*Resistance2_35C)/L;       %sample 2 resistivity
S2_35C_initial=ones(1802865,1)*3.5732e-6;
percent_S235C=(((Resistivity2_35C-S2_35C_initial)./S2_35C_initial)*100);
Resistance3_35C;
Resistivity3_35C=(A3_35C*Resistance3_35C)/L;       %sample 3 resistivity
S3_35C_initial=ones(1802865,1)*4.2751e-6;
percent_S335C=(((Resistivity3_35C-S3_35C_initial)./S3_35C_initial)*100);
StaticResistance_35C;
StaticResistivity_35C=(A4_35C*StaticResistance_35C)/L;%static resistivity 4
S4_35C_initial=ones(1802865,1)*4.2497e-6;
percent_S435C=(((StaticResistivity_35C-S4_35C_initial)./S4_35C_initial)*100);
%*****************************Initial Test Definitions*********************
Resistance_first_test;
Resistivity_first_test=(A_first_test*Resistance_first_test)/L;
Resistivity_first_test_initial=ones(3800507,1)*1.7999e-6;
percent_first_test=(((Resistivity_first_test-
Resistivity_first_test_initial)./Resistivity_first_test_initial)*100);
%*********************************************************************
```

APPENDIX 4: Additional Cross-sectional SEM and EDS Data

Cross sectional SEM and EDS reveal an amorphous silver nanoparticle phase in which the peak intensity of the Cl, lower left spectra, is within the instrumentations limit for reliably identifying the suspected presence of elemental Cl. Additionally, the crystalline Cl previously identified had a peak location much closer to the Ag peak and is noticeable absent in cross section.

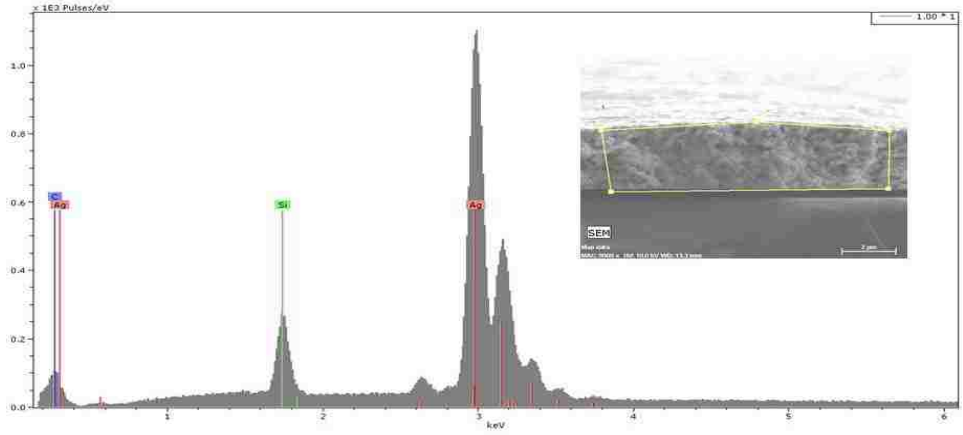

An un-sintered AJ deposition of silver nanoparticle ink did not indicate the presence of Cl in any form. While the sensing depth of the detection equipment is unknown and cross sectional SEM of an un-sintered sample not performed, the possibility that Cl evolves in the sintering process is supported by the figure below.

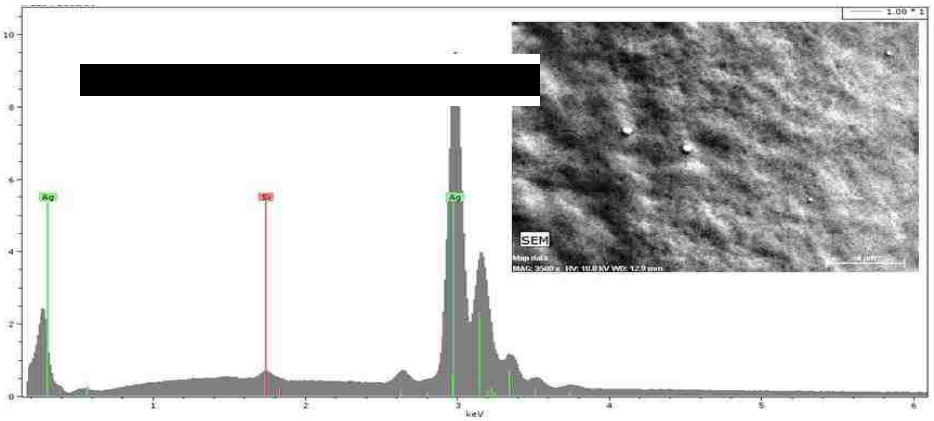

APPENDIX 5: Selection of 20 mA Sample Current

Specific information and geometries are proprietary to photovoltaic manufacturers and certain estimations must be made when specific data not available. Utilizing the specifications provided for a Sharp ND-N2ECU photovoltaic array and estimation of the current collector grid spacing, it was possible to make a reasonable approximation of the maximum current that any individual collector line would experience during normal operation of the assembled photovoltaic cell[29]. As an array is comprised of many individual cells, two common Bus Bars transfer current to from each individual cell to a central point. The current collecting grid is thus made up of what can be approximated as discrete line segments than span the width of a cell and transfer the generated current from the cell to the two Bus Lines. Physically measured (undisclosed source) collector grid spacing indicated that 1-2 millimeter spacing was currently supported by industry. The figure below depicts the geometry and calculation used to determine the maximum real world current input to an individual collector line.

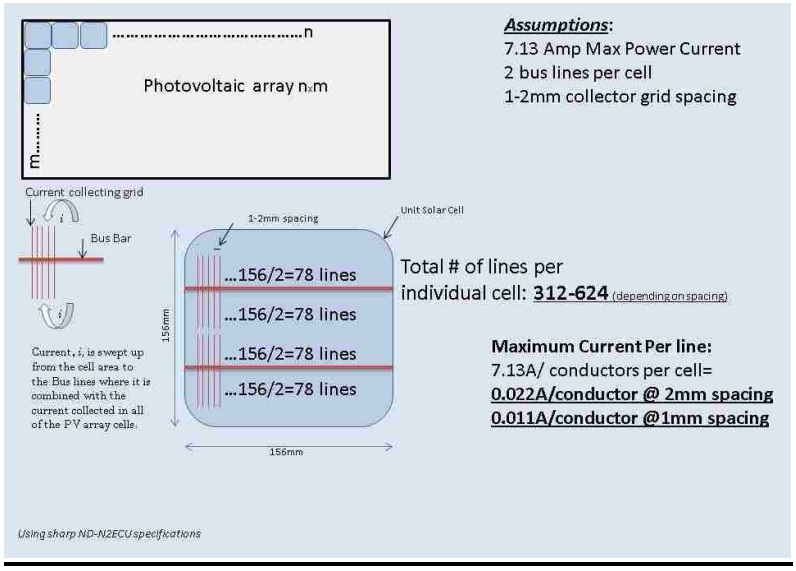

References:

(1) Galagan, Y.; Zimmermann, B.; Coenen, E. W. C.; Jorgensen, M.; Tanenbaum, D. M.; Krebs, F. C.; Gorter, H.; Sabik, S.; Sloff, L. H.; Vennstra, S. C.; Kroon, J. M.; Andriessen, R. *Advanced Energy Materials* **2012**, 103.

(2) Lee, J.; Lakshminarayan, N.; Dhungel, S. K.; Kim, K.; Yi, J. *Solar Energy Materials and Solar Cells* **2009**, *93*, 256.

(3) Rentsch, J.; Huljic, D. M.; Reber, S.; Preu, R.; Ludemann, R. In *Photovoltaic Specialists Conference, 2002. Conference Record of the Twenty-Ninth IEEE* 2002, p 134.

(4) Ju, M.; Lee, Y.-J.; Lee, J.; Kim, B.; Ryu, K.; Choi, K.; Song, K.; Lee, K.; Han, C.; Jo, Y.; Yi, J. *Solar Energy Materials and Solar Cells* **2012**, *100*, 204.

(5) Teng, K. F.; Vest, R. W. *Components, Hybrids, and Manufacturing Technology, IEEE Transactions on* **1988**, *11*, 291.

(6) Sun, J.; Ng, J. H.; Fuh, Y. H.; Wong, Y. S.; Loh, H. T.; Xu, Q. *Microsyst. Technol.* **2009**, *15*, 1437.

(7) Sungchul, J.; Baldwin, D. F. *Electronics Packaging Manufacturing, IEEE Transactions on* **2010**, *33*, 129.

(8) Dots, U. T. Champaign, IL, 2012, p http://www.utdots.com/page5.html.

(9) King, B. H.; O'Reilly, M. J.; Barnes, S. M. In *Photovoltaic Specialists Conference (PVSC), 2009 34th IEEE* 2009, p 001107.

(10) Zhao, D.; Liu, T.; Park, J. G.; Zhang, M.; Chen, J.-M.; Wang, B. *Microelectronic Engineering* **2012**, *96*, 71.

(11) Kahn, B. E. *Organic and Printed Electronics (2007), pp. 14-17 Key: citeulike:5645069* **2007**, *1*, 14.

(12) Horteis, M.; Glunz, S. W. *Progress in Photovoltaics: Research and Applications* **2008**, 555.

(13) Mette, A.; Richter, P. L.; Horteis, M.; Glunz, S. W. *Progress in Photovoltaics: Research and Applications* **2007**, 621.

(14) Kucharczyk, P.; Sharaf, M.; Münstermann, S. *International Journal of Fatigue* **2012**, *41*, 83.

(15) Nagesha, A.; Goyal, S.; Nandagopal, M.; Parameswaran, P.; Sandhya, R.; Mathew, M. D.; Mannan, S. K. *Materials Science and Engineering: A* **2012**, *546*, 34.

(16) Halonen, E.; Pynttäri, V.; Lilja, J.; Sillanpää, H.; Mäntysalo, M.; Heikkinen, J.; Mäkinen, R.; Kaija, T.; Salonen, P. *Microelectronic Engineering* **2011**, *88*, 2970.

(17) Wang, T.; Chen, G.; Wang, Y.; Chen, X.; Lu, G.-q. *Materials Science and Engineering: A* **2010**, *527*, 6714.

(18) Martynenko, E.; Zhou, W.; Chudnovsky, A.; Li, R. S.; Poglitsch, L. *Journal of Electronic Packaging* **2002**, *124*, 254.

(19) Wiese, S.; Meier, R.; Kraemer, F. In *Thermal, Mechanical & Multi-Physics Simulation, and Experiments in Microelectronics and Microsystems (EuroSimE), 2010 11th International Conference on* 2010, p 1.

(20) Quintero, J. A.; Mancosu, R. D.; de Oliveira, A. W. C.; Rolim, D. C.; da Silva, O. C.; Silva, J. M. In *Electronics Packaging Technology Conference, 2009. EPTC '09. 11th* 2009, p 1000.

(21) Lee, D. J.; Oh, J. H.; Bae, H. S. *Materials Letters* **2010**, *64*, 1069.

(22) Alastalo, A. T.; Mattila, T.; Allen, M. L.; Aronniemi, M. J.; Leppäniemi, J. H.; Ojanperä, K. A.; Suhonen, M. P.; Seppä, H. *MRS Proceedings* **2008**, *1113*.

(23) Maiwald, M.; Werner, C.; Zoellmer, V.; Busse, M. *Sensors and Actuators A: Physical* **2010**, 198.

(24) Yao, D.; Shang, J. K. *Acta Metallurgica et Materialia* **1994**, *42*, 589.

(25) Fox, L.; Sofia, J.; Shine, M. *Components, Hybrids, and Manufacturing Technology, IEEE Transactions on* **1985**, *8*, 275.

(26) Cole Jr., E. I. In *Microelectronics Failure Analysis Desk Reference, Sixth Edition*; Ross, R. J., Ed.; ASM International: 20111, p 246.

(27) Qi, H.; Alexson, D. A.; Glembocki, O. J.; Porokes, S. M. *Quantum Dots and Nanostructures: Synthesis, Characterization, and Modeling VIII* **2011**, *7947*.

(28) Stafford, R.; In *curvature and radius of curvature of a plane curve* 2007; Vol. 2012, p http://www.mathworks.com/matlabcentral/newsreader/view_thread/152405.

(29) Sharp_Electronics_Corporation ND-N2ECU Vol. 2012, p http://www.abcsolar.com/pdf/sol_dow_142W_SS.pdf.